*Research Article*

# A Novel Class of Inferior Colliculus Principal Neurons Labeled in Vasoactive Intestinal Peptide-Cre Mice

*David Goyer[1], Marina A. Silveira[1], Alexander P. George[1], Nichole L. Beebe[2], Ryan M. Edelbrock[2], Peter T. Malinski[1], Brett R. Schofield[2], Michael T. Roberts[1,*]*

[1]Kresge Hearing Research Institute, Department of Otolaryngology – Head and Neck Surgery, University of Michigan, Ann Arbor, Michigan 48109

[2]Department of Anatomy and Neurobiology, Northeast Ohio Medical University, Rootstown, Ohio 44272

*Corresponding author: microb@umich.edu

**Abstract**

Located in the midbrain, the inferior colliculus (IC) is the hub of the central auditory system. Although the IC plays important roles in speech processing, sound localization, and other auditory computations, the organization of the IC microcircuitry remains largely unknown. Using a multifaceted approach in mice, we have identified vasoactive intestinal peptide (VIP) neurons as a novel class of IC principal neurons. VIP neurons are glutamatergic stellate cells with sustained firing patterns. Their extensive axons project to long-range targets including the auditory thalamus, auditory brainstem, superior colliculus, and periaqueductal gray. Using optogenetic circuit mapping, we found that VIP neurons integrate input from the contralateral IC and the dorsal cochlear nucleus. The dorsal cochlear nucleus also drove feedforward inhibition to VIP neurons, indicating that inhibitory circuits within the IC shape the temporal integration of ascending inputs. Thus, VIP neurons are well-positioned to influence auditory computations in a number of brain regions.

## Introduction

The inferior colliculus (IC) is the hub of the central auditory pathway. Nearly all ascending output from the lower auditory brainstem and a large descending projection from the auditory cortex converge in the IC (Adams, 1979; Glendenning and Masterton, 1983; Oliver, 1987, 1984; Winer et al., 1998). In turn, the IC provides the main auditory input to the thalamocortical system (Calford and Aitkin, 1983). Neurons in the IC exhibit selective responses to the spectral and temporal content of sounds and perform computations important for sound localization and the identification of speech and other communication sounds (Felix et al., 2018; Winer and Schreiner, 2005). Despite these critical functions, we have limited knowledge about the organization and function of neural circuits in the IC. This is because probing neural circuits requires the ability to identify and manipulate specific classes of neurons, but IC neurons have proven difficult to delineate into distinct classes.

Anatomical studies have shown that IC neurons have disc-shaped or stellate morphologies (Malmierca et al., 1993; Meininger et al., 1986; Oliver and Morest, 1984). Disc-shaped neurons maintain their dendritic arbors within isofrequency lamina and make up the majority of neurons in the tonotopically organized central nucleus of the IC (ICc). Stellate neurons in the ICc extend their dendritic arbors across lamina and are therefore thought to integrate information across sound frequencies (Oliver et al., 1991). Both disc-shaped and stellate cells can be glutamatergic or GABAergic, an indication that each of these morphological groups consists of at least two neuron types (Oliver et al., 1994). Based on soma size and extracellular markers, IC GABAergic neurons have been divided into four classes (Beebe et al., 2016). Among these, “large GABAergic” neurons are the one consistently identified neuron type in the IC (Geis and Borst, 2013; Ito et al., 2015, 2009; Ito and Oliver, 2012). However, there are currently no known molecular markers specific for large GABAergic neurons (Schofield and Beebe, 2018).

Defining IC neuron types based on physiology has also proven difficult. IC neurons exhibit diverse responses to tones, but a comprehensive study showed that these responses form a continuum and cannot be used on their own to define functionally significant groups of neurons (Palmer et al., 2013). In addition, disc-shaped neurons could not be divided into distinct groups by matching their morphology with their in vivo physiology (Wallace et al., 2012). Similarly, GABAergic and glutamatergic IC neurons exhibit overlapping and equally diverse responses to sounds (Ono et al., 2017). In vitro recordings have shown that IC neurons exhibit diverse firing patterns, but these firing patterns do not correlate with neuronal morphology or neurotransmitter phenotype (Ono et al., 2005; Peruzzi et al., 2000; Reetz and Ehret, 1999; Sivaramakrishnan and Oliver, 2001).

In many brain regions, a multidimensional analysis that includes molecular markers has proven key to identifying neuron classes (Petilla Interneuron Nomenclature Group et al., 2008; Tremblay et al., 2016; Zeng and Sanes, 2017). Here, by combining molecular, morphological, and physiological analyses, we identify vasoactive intestinal peptide (VIP) neurons as a novel class of IC principal neurons. Our results show that VIP neurons are glutamatergic stellate neurons, are present in the major subdivisions of the IC, and are labeled in the VIP-IRES-Cre mouse line. Using viral tract tracing, we found that VIP neurons project to multiple auditory and non-auditory areas, demonstrating that a single neuron class can participate in most of the major projection pathways out of the IC. Using Channelrhodopsin-assisted circuit mapping (CRACM), we found that VIP neurons integrate input from the contralateral IC and the auditory brainstem. Input from the auditory brainstem also drove local, feedforward inhibition onto VIP neurons. Thus, our data reveal a novel circuit motif that may control the temporal summation of ascending input to the IC. Together, these results represent a critical step toward determining how defined neural circuits in the IC support sound processing.

67 **Results**

68 **The VIP-IRES-Cre mouse line labels neurons in multiple subdivisions of the IC**

69 By crossing VIP-IRES-Cre mice with Ai14 reporter mice, we obtained mice in which VIP$^+$ neurons
70 expressed the fluorescent protein tdTomato. VIP$^+$ neurons in these animals were visible in numerous
71 brain regions; the present report focuses on the IC. **Figure 1** shows the distribution of VIP$^+$ neurons
72 (magenta) in transverse sections through the IC. Labeled neurons were present throughout most of the
73 rostro-caudal extent of the IC, but were most numerous in the caudal regions. Labeled neurons were
74 rare or absent in the IC rostral pole and intercollicular tegmentum.

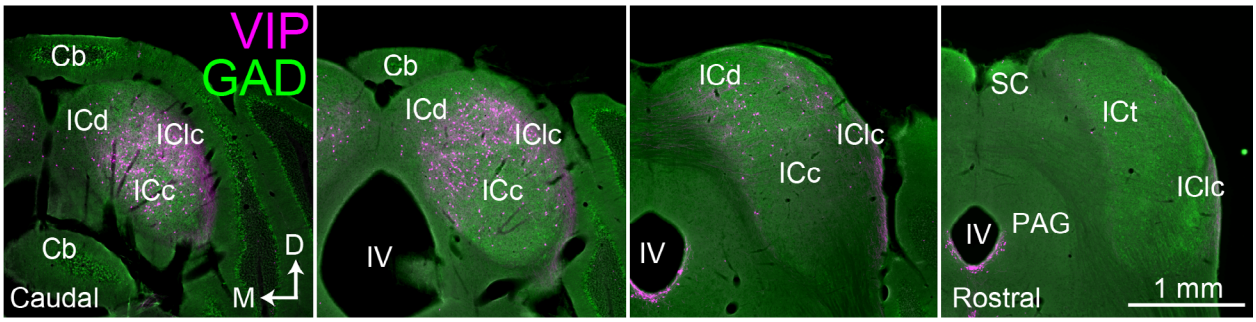


75

**Figure 1. VIP neurons are distributed across multiple subdivisions of the IC.** Photomicrographs of transverse sections through the IC ranging from caudal (left-most) to rostral (right-most). VIP-expressing cells (labeled with tdTomato) are shown in magenta, and GAD67 staining is shown in green to show the border of the IC. VIP-expressing cells are present in multiple subdivisions of the IC, but are most prominent in caudal and dorsal parts of the IC. Scale = 1 mm. Cb (cerebellum), ICc, ICd, IClc (central nucleus, dorsal cortex and lateral cortex of the inferior colliculus), ICt (intercollicular tegmentum), IV (fourth ventricle), PAG (periaqueductal gray).

76 **VIP neurons are glutamatergic and represent 1.8% of IC neurons**

77 Previous studies have shown that IC neurons are either glutamatergic or GABAergic (Merchán et al.,
78 2005; Oliver et al., 1994). To investigate the neurotransmitter content of VIP neurons, we performed
79 immunohistochemical staining against GAD67, a marker for GABAergic neurons, in brain slices from
80 three VIP-IRES-Cre x Ai14 animals, aged P58 (**Figure 2A**). We then counted tdTomato$^+$ neurons and
81 GAD67-labeled cell bodies in one caudal and one rostral IC slice per animal. Neurons located in the ICc,
82 ICd, and IClc were combined for this analysis. Across 793 tdTomato$^+$ neurons, only 10 neurons co-

**Table 1. VIP neurons are glutamatergic.** Across three mice, an average of 1.3% of tdTomato$^+$ neurons were labeled with an antibody against GAD67.

| Animal | Slice # | # tdTomato$^+$ | # GAD67$^+$ | # co-labeled | % tdTomato$^+$ co-labeled |
|---|---|---|---|---|---|
| **P58 female, #1** | 1 (caudal) | 210 | 184 | 3 | 1.4 |
| | 2 (middle) | 172 | 65 | 2 | 1.2 |
| | **Total** | **382** | **249** | **5** | **1.3** |
| **P58 male** | 1 (caudal) | 151 | 152 | 2 | 1.3 |
| | 2 (middle) | 46 | 212 | 2 | 4.3 |
| | **Total** | **197** | **364** | **4** | **2.0** |
| **P58 female, #2** | 1 (caudal) | 161 | 137 | 0 | 0.0 |
| | 2 (middle) | 53 | 187 | 1 | 1.9 |
| | **Total** | **214** | **324** | **1** | **0.5** |
| | **Grand total** | **793** | **937** | **10** | **1.3** |
| | | | | **Average across 3 mice (mean ± SD)** | **1.3 ± 0.8%** |

labeled with GAD67 (1.3%, **Table 1**). These data suggest that VIP neurons are a subgroup of glutamatergic neurons in the IC.

To determine the percentage of IC neurons that are VIP neurons, we performed immunostaining with anti-NeuN, a neuron-selective antibody previously shown to label most or all neurons in the IC (Beebe et al., 2016; Foster et al., 2014; Mellott et al., 2014) (**Figure 2B**). Coronal IC sections from two VIP-IRES-Cres x Ai14 mice were stained, and three sections per mouse were analyzed: one caudal, one middle, and one rostral. To ensure unbiased counting of neurons, we applied the optical fractionator method, a design-based stereology approach (see Materials and Methods; West et al., 1991). The ICc, ICd, and IClc were combined for this analysis. Accordingly, we used systematic random sampling to collect confocal image stacks at evenly spaced intervals from each IC section. Each image stack was inspected to determine the boundaries of the slice, and guard zones were set at the top and bottom of the slice to delineate a central, 15 µm-thick section of the slice for subsequent analysis. Within this 15

95 µm-thick region, we separately marked NeuN$^+$ neurons and tdTomato$^+$ neurons, then overlaid the NeuN
96 and tdTomato images to determine the number of double-marked cells. Across six slices from 2 mice,
97 we found that 1.8% of neurons in the mouse IC are VIP neurons (205 of 11,175 neurons counted,
98 **Table 2**).

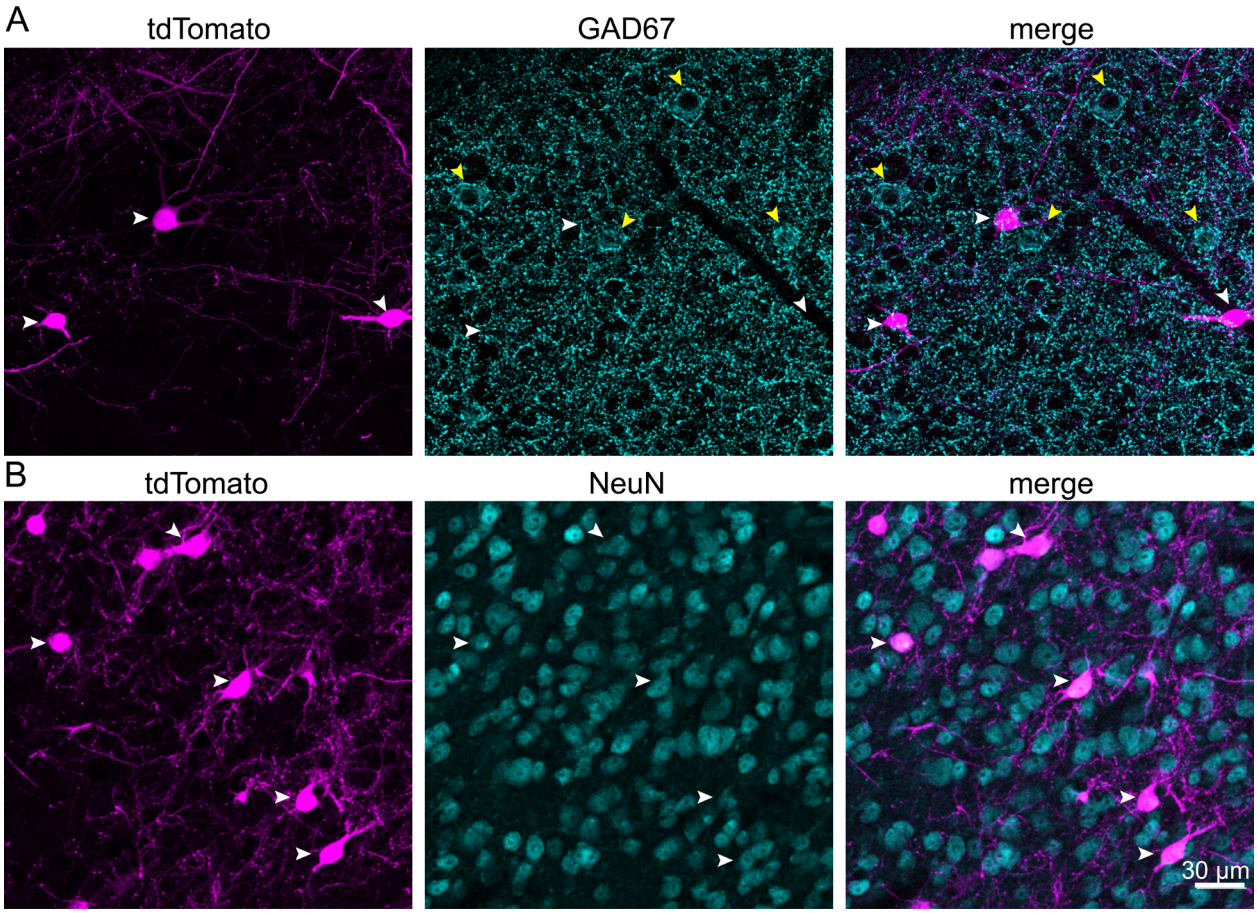


99

**Figure 2. VIP neurons are glutamatergic and represent 1.8% of the total neuronal population in the IC. (A)** Confocal z-stack projections showing IC VIP neurons (magenta, left), GAD67 staining (cyan, middle), and an overlay (right). White arrowheads mark VIP neurons, yellow arrowheads GABAergic cell bodies. There was virtually no overlap between VIP neurons and GABAergic neurons (right). **(B)** Confocal z-stack projections showing VIP neurons (magenta, left), NeuN staining (cyan, middle), and an overlay (right). White arrowheads mark VIP neurons labeled by NeuN. Scale bar applies to A and B.

100

**Table 2. VIP neurons represent 1.8% of the total population of IC neurons.** Table shows results from stereological analysis of the percentage of IC neurons ($NeuN^+$) that express tdTomato in VIP-IRES-Cre x Ai14 mice. Values indicate mean ± SEM, (#$tdTomato^+$ neurons /#$NeuN^+$ neurons), and number of systematic random samples analyzed from each slice.

| Slice plane | P58 male | P80 female | Per slice plane | Grand Average |
|---|---|---|---|---|
| **Caudal** | 1.9 ± 0.8 %<br>(26/1356)<br>6 samples | 2.8 ± 0.9 %<br>(67/2381)<br>14 samples | 2.4 ± 0.4 %<br>(93/3737) | |
| **Middle** | 0.9 ± 0.3 %<br>(12/1389)<br>10 samples | 1.9 ± 0.6 %<br>(34/1825)<br>9 samples | 1.4 ± 0.5 %<br>(46/3214) | |
| **Rostral** | 1.6 ± 0.4 %<br>(30/1887)<br>10 samples | 1.5 ± 0.3 %<br>(36/2337)<br>16 samples | 1.6 ± 0.02 %<br>(66/4224) | |
| **Per mouse** | 1.5 ± 0.3 %<br>(68/4632) | 2.1 ± 0.4 %<br>(137/6543) | | 1.8 ± 0.3 %<br>(205/11,175) |

## VIP neurons exhibit sustained firing patterns and their intrinsic physiology varies along the tonotopic axis of the ICc

Next, we investigated the firing pattern and intrinsic physiology of VIP neurons by targeting whole cell patch clamp recordings to $tdTomato^+$ neurons in brain slices from VIP-IRES-Cre x Ai14 mice. Recordings made from the ICc, ICd, and IClc were lumped together for this experiment because there were no clear differences in VIP neuron physiology across these subdivisions of the IC. VIP neurons had a resting membrane potential of -69.5 mV ± 4.4 mV (n = 216, corrected for liquid junction potential). In response to a current step protocol with hyperpolarizing and depolarizing current injections, VIP neurons showed minimal to no voltage sag to hyperpolarizing current steps and a sustained firing pattern of action potentials to depolarizing current steps (**Figure 3$A_1$, $A_2$**). Neurons were classified as sustained if their spike frequency adaptation ratio (SFA) was less than 2 (Peruzzi et al., 2000). The SFA ratio was calculated by dividing the last interspike interval by the first for a depolarizing current step that elicited ~10 spikes. 90.3% (214 of 237) of patched VIP neurons exhibited a sustained firing pattern, 8.4% (20 of 237) showed

an adapting firing pattern (SFA ratio >= 2), and 1.3% (3 of 237) of VIP neurons had a strongly adapting firing pattern (firing stopped before the end of the current step).

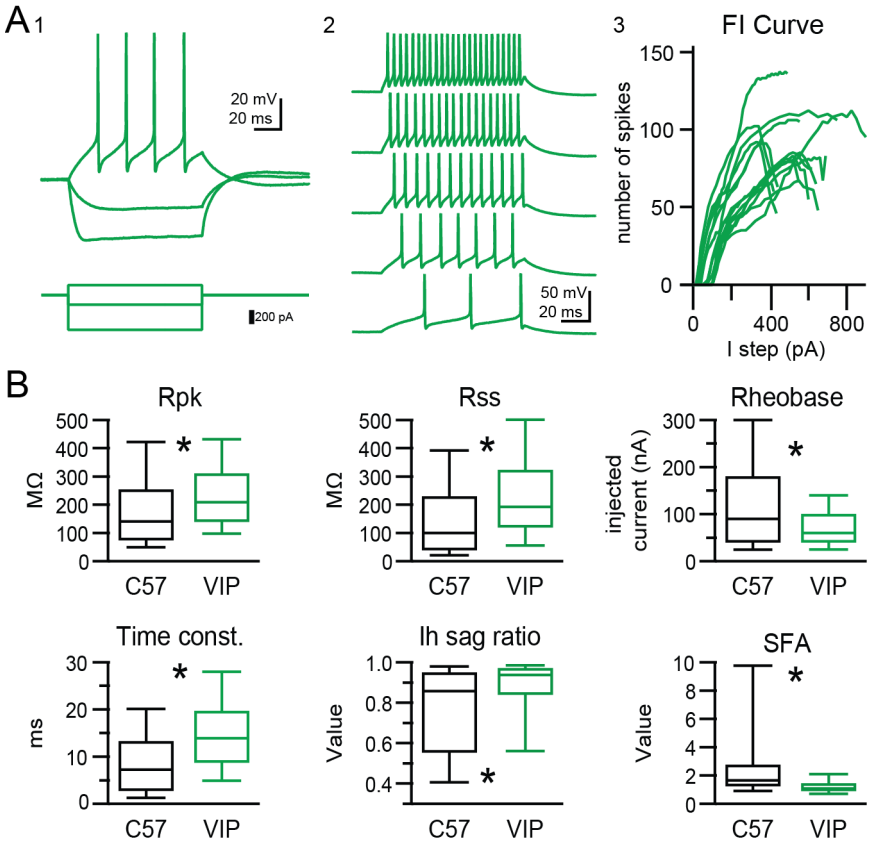


**Figure 3. VIP neurons have sustained firing patterns and moderate membrane properties. (A)** VIP neurons exhibited a regular, sustained firing pattern in response to depolarizing current steps, while hyperpolarizing current steps elicited minimal voltage sag (A1). As the amplitude of depolarizing current steps was increased, VIP neurons increased their firing rate while keeping their sustained firing pattern (A2). Example firing versus input (FI) curves from 15 VIP neurons show that firing rate increased in a mostly linear fashion over a broad range of current step amplitudes (A3). **(B)** Intrinsic physiology of VIP neurons is statistically different from the general population of IC neurons for all parameters tested. On average, VIP neurons had a significantly higher peak input resistance ($R_{pk}$) and steady-state input resistance ($R_{ss}$), a lower rheobase, a longer membrane time constant, a smaller and less variable voltage sag ($I_h$) at -91 mV, and a markedly small and highly invariable spike frequency adaptation ratio (SFA). Boxplots show median, 25$^{th}$ and 75$^{th}$ percentile (box), and 9$^{th}$ and 91$^{th}$ percentile (whiskers).

To compare the physiology of VIP neurons to that of the general population of neurons in the IC, we patched neurons in IC slices of C57BL/6J mice in a random, non-targeted approach as a control. Neurons patched with the non-targeted (NT) approach showed a higher diversity in firing patterns, with a higher proportion of strongly adapting neurons (21.8%, 12 out of 55) and adapting neurons (16.4%, 9 out of 55) when compared to VIP neurons. Sustained firing neurons were the most prevalent group in

NT recordings (58.2%, 32 out of 55). Additionally, 3.6% (2 of 55) of randomly patched IC neurons fired only 1 spike at the onset of the depolarizing current step. This firing pattern was never observed in VIP neurons. The intrinsic physiology of VIP neurons also differed significantly from the general population of IC neurons (see **Figure 3B**). VIP neurons on average had a higher peak input resistance ($R_{pk}$) than non-targeted neurons (mean ± SD: VIP 242.1 ± 139.4 MΩ vs NT 191.1 ± 161.4 MΩ, p=0.0003, Wilcoxon rank sum test), a higher steady-state input resistance ($R_{ss}$) (mean ± SD: VIP 239.7 ± 170.7 MΩ vs NT 153.4 ± 153.2, p = 0.0001, Wilcoxon rank sum test), a slower membrane time constant (mean ± SD: VIP 15.0 ± 8.8 ms vs NT 9.7 ± 7.6 MΩ, p = $6.8*10^{-7}$, Wilcoxon rank sum test), lower rheobase values (mean ± SD: VIP 67.8 ± 96.2 pA vs NT 120.0 ± 100.9 pA, p = 0.013, Wilcoxon rank sum test), and a much less pronounced voltage sag (mean ± SD: VIP 0.87 ± 0.16 vs NT 0.75 ± 0.21, p = 0.0003, Wilcoxon rank sum test). Most striking, the SFA ratio of VIP neurons was tightly clustered at 1.47 ± 1.62, whereas SFA of NT neurons showed a significantly higher value and spread (3.62 ± 5.43, mean ± SD, p = $2.07*10^{-7}$).

Although statistically different from the general neuronal population in the IC and showing a tightly clustered SFA ratio, the intrinsic physiology of VIP neurons still showed some level of variability. In the lower auditory brainstem, it has been found that the intrinsic physiology of some neurons varies along the tonotopic axis (Baumann et al., 2013; Hassfurth et al., 2009). We therefore hypothesized that the intrinsic physiology of VIP neurons in the ICc varied along the tonotopic axis of the ICc. During patch clamp experiments, VIP neurons were passively filled with biocytin via the internal solution. Slices were fixed and stained post hoc with a streptavidin-Alexa Fluor conjugate (see Materials and Methods). We then used confocal imaging to map the location of the recorded neurons relative to a two-dimensional (medial-lateral and dorsal-ventral) coordinate system superimposed on the left IC (n = 61 neurons; **Figure 4A**). Correlations between intrinsic physiology and location in the ICc were tested by fitting a plane to scatter plots of intrinsic parameters versus medial-lateral and dorsal-ventral coordinates

(**Figure 4B**). Because the ICd and IClc are not tonotopically organized, only neurons located in the ICc were included in this analysis.

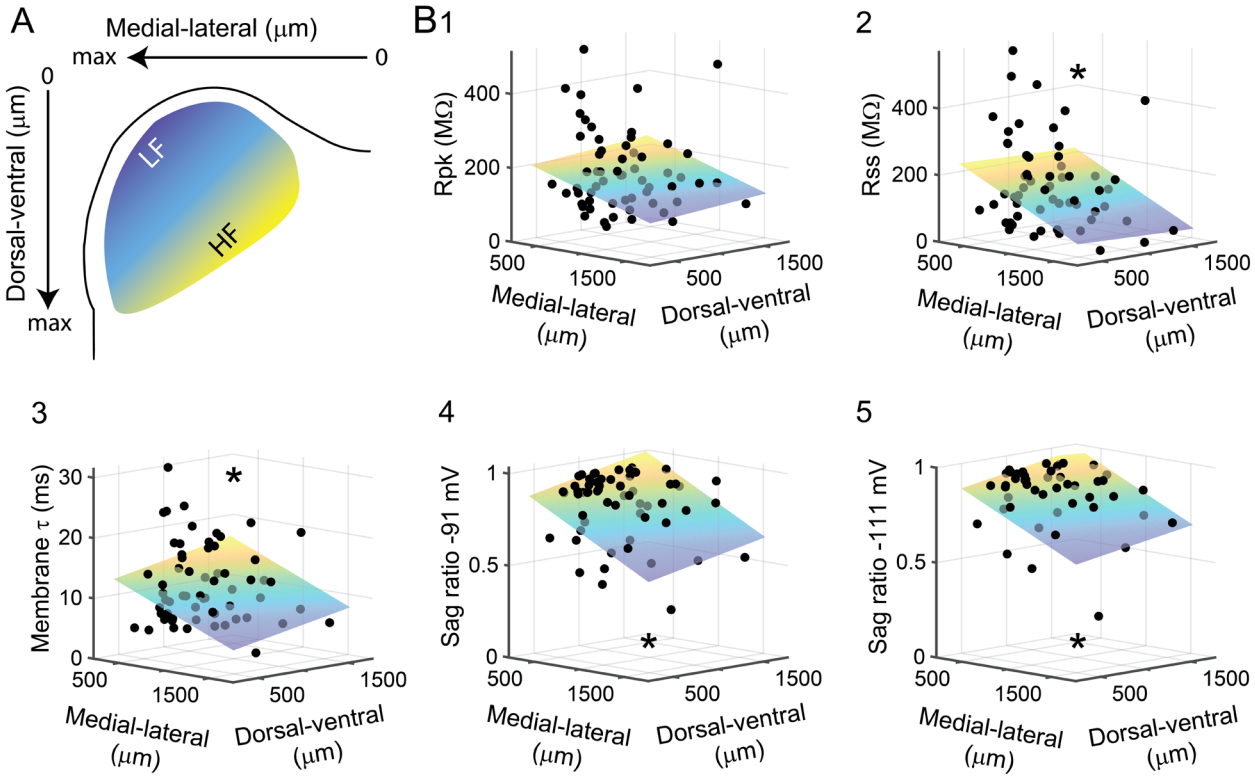


**Figure 4. Intrinsic physiology of VIP neurons in the ICc varies along the tonotopic axis. (A)** A 2D coordinate system was fit to every IC slice a VIP neuron was recorded from. The medial-lateral axis runs from the midline (zero) to the lateral edge (max) of the slice, the dorsal-ventral axis from the dorsal edge of the slice (zero) to the ventral border of the IC (max). For illustrative purposes, the approximate position along the tonotopic axis of the ICc is color-coded from blue (low frequency) to yellow (high frequency). **(B)** Correlation of measured intrinsic parameters with recording location. Black dots represent physiological parameters of individual VIP neurons (z-axis, left) mapped to their recording location (x- and y-axes, bottom). Planes show Levenberg-Marquardt least squares fits, color-coded from low z-axis values (blue) to high z-axis values (yellow). Asterisks indicate statistical significance of fit.

We found that variability in the intrinsic physiology of VIP neurons was at least partially correlated to their location within the coronal plane of the ICc. This was particularly true for the voltage sag ratios, which measure hyperpolarization-activated cation current ($I_h$). Approximately one quarter of the variability in sag ratios was explained by location in the ICc (sag ratio at -91 mV: R = 0.536, $R^2_{adj}$ = 0.262, p = 1.24 x $10^{-05}$, n = 60, **Figure 4B$_4$**; sag ratio at -111 mV: R = 0.516, $R^2_{adj}$ = 0.233, p = 0.0002, n = 47, **Figure 4B$_5$**). A significant but smaller portion of the variability in membrane time constant was explained by location in the ICc (τ: R = 0.343, $R^2_{adj}$ = 0.088, p = 0.007, n = 61; **Figure 4B$_3$**). There was also

a significant relationship between the steady-state input resistance of VIP neurons and location in the ICc and a trend toward a relationship between peak input resistance and location ($R_{ss}$: R = 0.328, $R^2_{adj}$ = 0.076, p = 0.011, n = 60; $R_{pk}$: R = 0.227, $R^2_{adj}$ = 0.018, p = 0.084, n = 60; **Figure 4B$_{1,2}$**). The tonotopic axis of the ICc runs along a dorsolateral (low frequency) to ventromedial (high frequency) axis (Malmierca et al., 2008; Portfors et al., 2011; Stiebler and Ehret, 1985; Willott and Urban, 1978). For each of the above intrinsic parameters, values tended to be lower, indicating faster membrane properties, at more dorsolateral locations and higher, indicating slower membrane properties, at more ventromedial locations. Combined, these results suggest that variability in the intrinsic physiology of VIP neurons is at least in part due to their localization along the tonotopic axis of the ICc and that the membrane properties of VIP neurons tend to be faster in lower frequency regions of the ICc.

## VIP neurons have stellate morphology and dendritic spines

The streptavidin staining of biocytin-filled VIP neurons allowed for a detailed analysis of morphology. In total, we recovered the morphology of 55% of patched VIP neurons (n = 100 of 183). Nearly all (81/86 = 94.2%) VIP neurons had spiny dendrites (**Figure 5A, B** insets). This contrasts sharply with the 28% (12 of 43 neurons) of neurons that had spiny dendrites in non-targeted recordings from C57BL/6J mice (**Figure 5C**), suggesting that VIP neurons represent a subset of IC cells. Nonetheless, dendritic spines can be present on a variety of cell types, including stellate and disc-shaped cells (Herrera et al., 1988; Paloff et al., 1992; Willard and Ryugo, 1983). On average, VIP neurons had 5 primary dendrites (mean ± SD: 4.77 ± 1.38) that spread out in all directions from the soma, consistent with a stellate morphology. This is unsurprising in the ICd and IClc, where stellate morphology predominates, but warranted further analysis in the ICc, where stellate cells can have oriented dendritic trees but are outnumbered by the

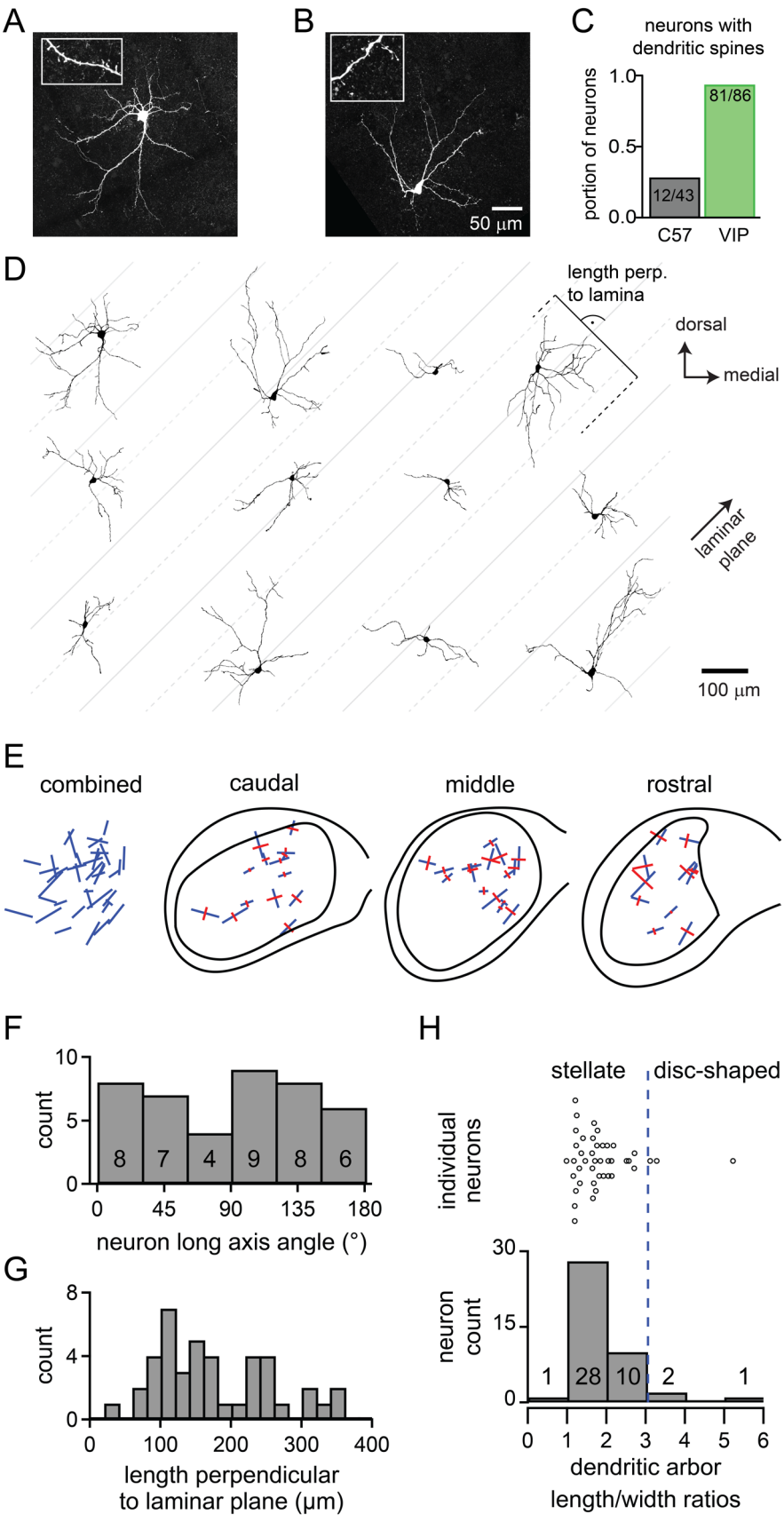


175

**Figure 5.** ***VIP neurons in the ICc are a class of stellate cells and most VIP neurons have dendritic spines. (A, B)*** *Maximum-intensity projections of confocal z-stacks showing streptavidin-Alexa Fluor-stained VIP neurons from the ICc. Insets: enlarged views of dendritic segments show dendritic spines.* ***(C)*** *94% of VIP neurons across all IC subdivisions had spiny dendrites vs 28% of neurons from non-targeted recordings in C57BL/6J animals.* ***(D)*** *Representative reconstructions of the morphology of 12 VIP neurons from the ICc. Neurons are oriented as if in the left ICc. Gray lines were drawn at a 45° angle to illustrate the general orientation of the laminae. Solid gray lines are spaced 200 µm apart, dashed lines and solid lines are spaced 100 µm apart.* ***(E)*** *Orientation of the dendritic fields of VIP neurons from the ICc. Combined: Orientation of all reconstructed VIP neurons from the ICc (n = 42). Blue lines denote the orientation of the longest axis (first principal direction) found for each neuron using 2D PCA. Caudal, middle, rostral: Orientation of dendritic fields separated according to position along the rostro-caudal axis of the ICc. Blue lines show longest axis, perpendicular red lines show second longest axis (second principal direction) of each neuron as defined by 2D PCA.* ***(F)*** *Angular orientation of the long axis for every reconstructed VIP neuron within the ICc. Angles indicate counter-clockwise rotation relative to the medial-lateral (horizontal) axis.* ***(G)*** *Spread of the dendritic arbors of ICc VIP neurons measured perpendicular to a predicted 45° isofrequency plane. The dendrites of 83% of VIP neurons extended more than 100 µm across the laminar plane.* ***(H)*** *Dendritic arbor length to width ratio for all reconstructed VIP neurons from the ICc (n = 42). 93% of VIP neurons had a length to width ratio < 3, indicating that they are stellate cells. The orientation of length and width axes was determined using 3D PCA.*

more highly oriented disc-shaped cells (Malmierca et al., 1993; Oliver and Morest, 1984; Willard and Ryugo, 1983).

**Figure 5D** shows the variability in the morphology of VIP neurons located in the ICc. Neurons are displayed as they would appear in a coronal slice of the left IC viewed from a caudal perspective. Oliver and colleagues distinguished disc-shaped from stellate neurons by calculating the length to width ratio of the dendritic arbor: neurons with a ratio <3 were stellate and those with a ratio >=3 were disc-shaped (Oliver et al., 1991). Applying this classification to our sample, 93% of VIP neurons in the ICc (39 of 42 neurons) had a length to width ratio <3, therefore being classified as stellate (**Figure 5H**). Only three VIP neurons from the ICc had a length to width ratio >3. These results demonstrate that the dendritic arbors of VIP neurons are not as highly oriented as disc-shaped neurons, again consistent with the hypothesis that VIP neurons are a class of stellate neurons.

Although less oriented than disc-shaped cells, the VIP dendrites tended to show some orientation that could influence the range of frequencies that converge on the cell. To measure the orientation of ICc VIP neurons in relation to the isofrequency laminae, which in mouse run in a ~45° angle through the ICc (Stiebler and Ehret, 1985), we identified the longest and second longest axis of

each neuron through principal component analysis and plotted the orientation of these axes on a standardized model of the IC (**Figure 5E**). No preferred orientation was apparent (**Figure 5E**, *combined*). Only 17% of VIP neurons (7 of 42) had their longest axis oriented within ± 15° of the 45° laminar plane, indicating that the dendritic arbors of most VIP neurons (83%, 35 of 42) may be positioned to cross one or more isofrequency laminae in the ICc (**Figure 5F**). To quantify this, we calculated the length the dendritic arbor extended perpendicular to a 45° laminar plane. The dendritic arbors of 83% of ICc VIP neurons (35 of 42) spread more than 100 µm perpendicular to the laminar plane, and more than 36% (15 of 42) spread more than 200 µm across the laminar plane (**Figure 5G**). Previous work in rats has shown that the isofrequency laminae have a center-to-center distance that ranges from 90 – 150 µm, while neurons contained within a lamina had a thickness ranging from 30 – 70 µm (Malmierca et al., 1993). If we assume that laminar dimensions in mouse are no thicker than those in rats, our results indicate that the dendritic fields of VIP neurons usually extend beyond at least one isofrequency lamina, consistent with the conclusion that VIP neurons in the ICc are a class of stellate neurons.

## VIP neurons project to targets within and beyond the IC

Injections of an AAV encoding a Cre-dependent eGFP construct, AAV1.CAG.FLEX.eGFP.WPRE.bGH, led to eGFP expression in $VIP^+$ IC cells. **Figure 6A** shows a representative deposit site, with eGFP-positive neurons (yellow) located among a population of $VIP^+$ cells (magenta, labeled by cross-breeding the VIP-IRES-Cre mice with Ai14 reporter mice). Neurons that expressed eGFP routinely co-expressed tdTomato, confirming VIP expression by those neurons (**Figure 6B**). Many $tdTomato^+$ neurons did not express the eGFP, despite their intermingling with many virally-labeled neurons. eGFP-labeled axons were prominent within the injected IC, where the labeled boutons were located in the neuropil or in close apposition to IC somas, suggesting extensive contributions to local circuits (**Figure 6C**). In addition, eGFP-labeled axons were present in several fiber tracts carrying projections from the IC, including the brachium of the IC, the commissure of the IC and the lateral lemniscus. Labeled axons and boutons were

found in numerous auditory nuclei, including the contralateral IC, medial geniculate body and superior olivary complex (**Figure 6D-F**). Additional targets included the nucleus of the brachium of the IC, the periaqueductal gray, and the superior colliculus (not shown; details of termination patterns and terminal axon morphology will be described in a subsequent report). These data indicate that VIP$^+$ IC neurons contribute to ascending, commissural and descending pathways from the IC.

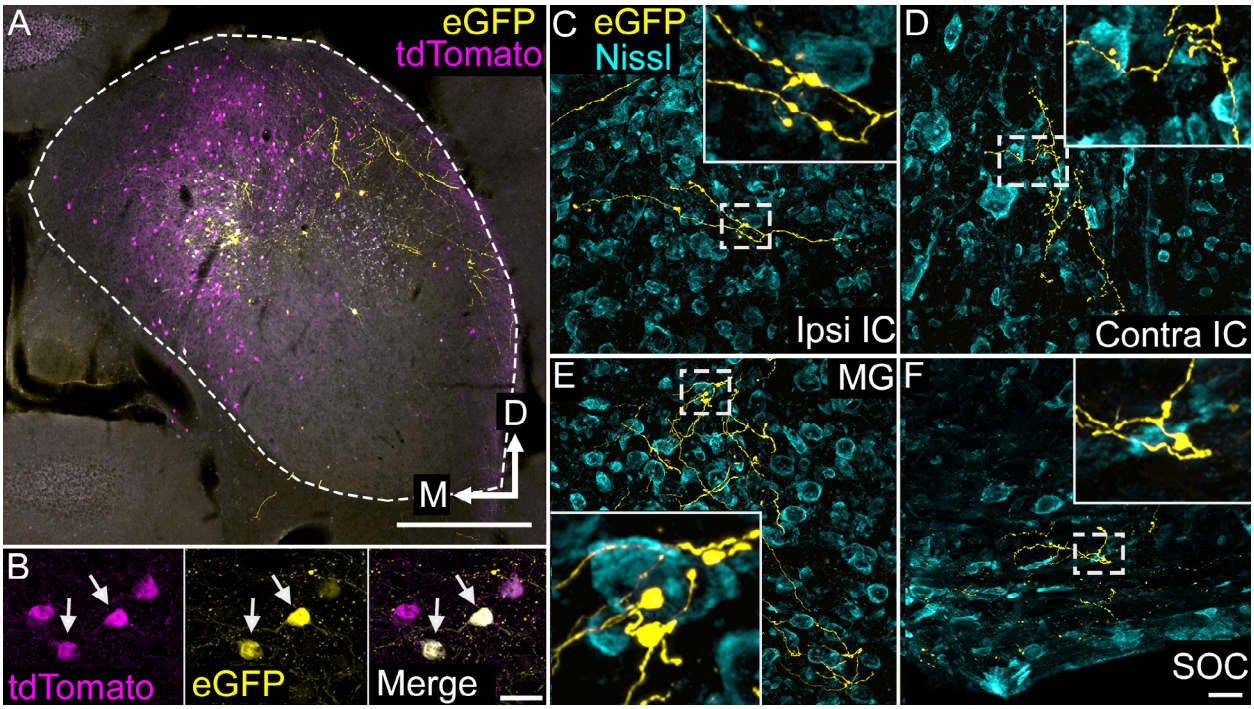


**Figure 6. VIP neurons project to multiple local and long-range targets. (A)** Photomicrograph of an AAV deposit site in the right IC. AAV-infected, VIP-expressing cells are labeled with eGFP (yellow), while all VIP-expressing cells are labeled with tdTomato (magenta). Cells expressing both fluorescent proteins appear white. Scale = 500 µm. **(B)** High magnification photomicrographs showing labeled cells in the AAV deposit site. The field shows four tdTomato-expressing cells (magenta), two of which (white arrows) were also AAV-infected and expressed eGFP (yellow). Scale = 20 µm. **(C-F)** High magnification photomicrographs showing eGFP-labeled collicular axons (yellow) terminating in the ipsilateral IC (C), the contralateral IC (D), the medial geniculate body (E), or the ventral nucleus of the trapezoid body in the superior olivary complex (F) after an AAV injection in the IC. The white dashed box in each image identifies an area enlarged in the inset to show details of labeled axons and boutons. A fluorescent Nissl stain (cyan) shows that boutons are located in close association with cell bodies as well as in the intervening neuropil. Scale = 20 µm

**VIP neurons in the ICc receive excitatory and inhibitory synaptic input from the contralateral IC**

In addition to axonal projection patterns, the sources of synaptic input to a neuron class are an important predictor of neuronal function. Anatomical studies have shown that the IC receives

ascending, descending, and commissural input, but, with the exception of large GABAergic neurons (Ito et al., 2015; Ito and Oliver, 2014), it has rarely been possible to identify the sources and physiology of synaptic input to a specific class of neurons in the IC. This is largely because axons from multiple sources overlap in the IC, making it difficult to use electrical stimulation to selectively activate axons from specific presynaptic sources. To overcome this obstacle, we turned to Channelrhodopsin-assisted circuit mapping (CRACM) (Petreanu et al., 2007). With CRACM, it is possible to selectively activate a single population of presynaptic neurons by anatomically and/or molecularly restricting the expression of an optogenetic protein.

Numerically, the contralateral IC provides the largest single source of input to the IC (Moore, 1988). We therefore first used CRACM to test whether VIP neurons in the ICc receive commissural input. Using stereotaxic, intracranial virus injections with AAV1.Syn.Chronos-GFP.WPRE.bGH, we drove expression of GFP-tagged Chronos, a fast Channelrhodopsin variant (Klapoetke et al., 2014), in the right IC. We then targeted recordings to VIP neurons in the contralateral (left) ICc (**Figure 7A**). In each experiment, we used GFP fluorescence to verify transfection of the right IC (**Figure 7B**) and restricted our recordings to VIP neurons in areas of the left ICc where GFP-labelled axons were visible. Because commissural projections are a mixture of glutamatergic and GABAergic projections (González-Hernández et al., 1996; Hernández et al., 2006; Nakamoto et al., 2013; Saint Marie, 1996), we used pharmacology to isolate EPSPs and IPSPs. Indeed, without adding receptor antagonists to the bath, postsynaptic potentials often were mixtures of IPSPs and EPSPs (data not shown). In the presence of AMPA and NMDA receptor antagonists (10 µM NBQX and 50 µM D-AP5, bath application), 2 – 5 ms flashes of blue light elicited IPSPs in 6 out of 12 neurons tested (**Figure 7C, left**). IPSPs were completely abolished by the $GABA_A$ receptor antagonist gabazine (5 µM, **Figure 7C, right**; n = 6; amplitude, p = 0.006; rise time, p = 0.003; halfwidth, p = 0.001; membrane time constant, p = 0.003, paired t-test). On average (n = 6), commissural IPSPs in ICc VIP neurons were small (-1.53 mV ± 0.96 mV) and had moderate 10 – 90% rise

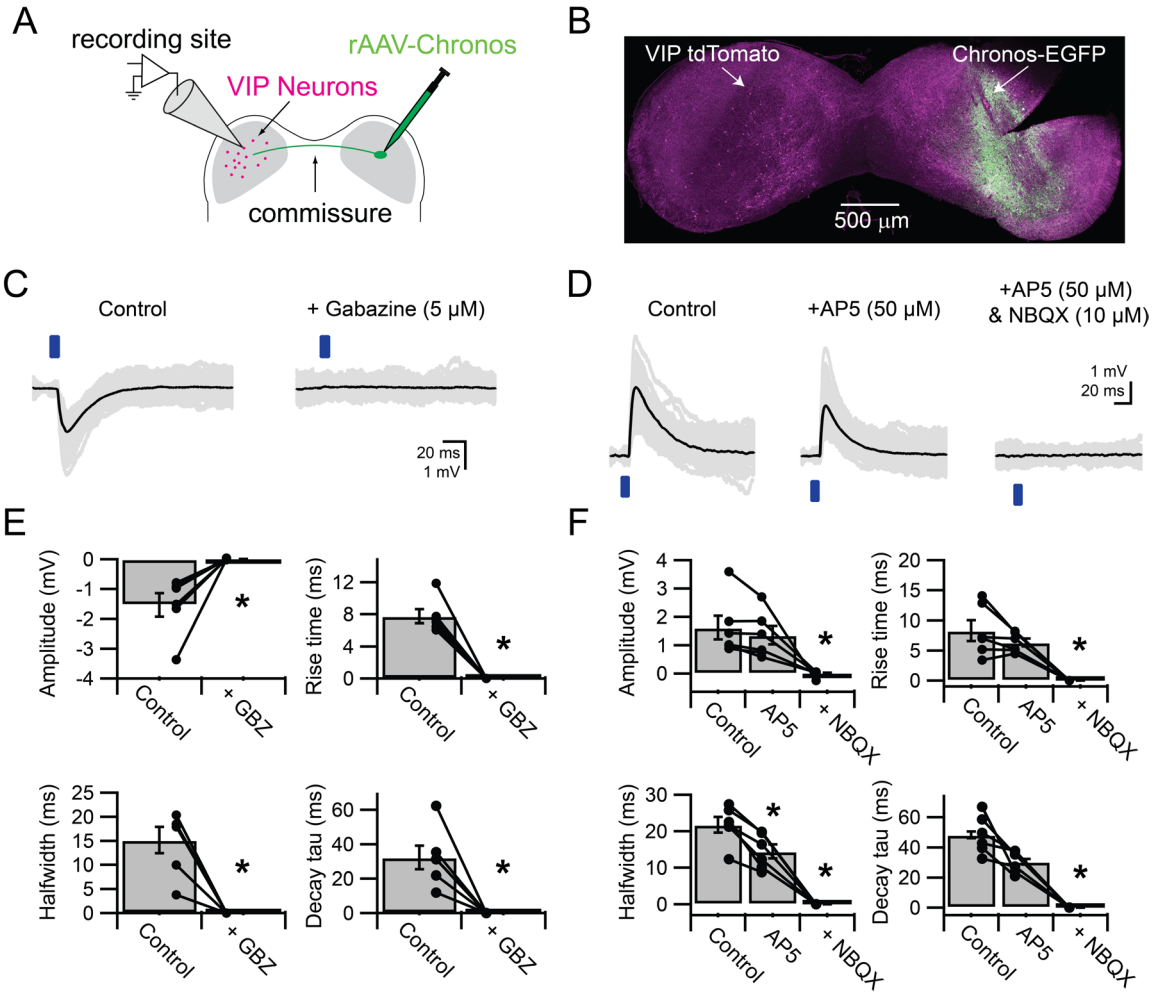


**Figure 7. VIP neurons in the ICc receive excitatory and inhibitory synaptic input from the contralateral IC. (A)** Experimental setup. An AAV encoding Chronos-GFP was injected into the right IC. Three weeks later, light-evoked postsynaptic potentials were recorded from VIP neurons in the left ICc. **(B)** Image of a coronal slice of the IC. Injection sites and Chronos expression were validated through Chronos-GFP fluorescence. **(C)** Optogenetically-evoked IPSPs recorded from VIP Neurons in the ICc contralateral to the AAV injection site. IPSPs were evoked by 2 – 5 ms blue light flashes (left), while EPSPs were blocked with NBQX and AP5. IPSPs were abolished by gabazine (right). **(D)** Optogenetically-evoked EPSPs recorded from VIP neurons in the ICc contralateral to the AAV injection site. EPSPs were evoked by 2 – 5 ms blue light flashes (left), while IPSPs were blocked with strychnine and gabazine. Wash-in of AP5 significantly reduced the halfwidth and decay time constant of light-evoked EPSPs (middle). Wash-in of NBQX abolished the remaining EPSP (right). **(E)** Population data showing amplitude and kinetics of optogenetically-evoked IPSPs. **(F)** Population data showing amplitude and kinetics of optogenetically-evoked EPSPs. The significant reduction of EPSP halfwidth by AP5 indicates that NMDA receptor activation prolonged EPSP duration.

times (7.8 ms ± 2.1 ms), halfwidths (15.1 ms ± 6.8 ms) and decay time constants (32.4 ms ± 17.0 ms) (**Figure 7E**).

To investigate excitatory commissural inputs to ICc VIP neurons, recordings were carried out in the presence of $GABA_A$ and glycine receptor antagonists (5 µm gabazine and 1 µM strychnine, bath application, **Figure 7D**). We found that 2 – 5 ms flashes of blue light elicited EPSPs in 11 out of 27 neurons (**Figure 7D, left**). On average (n = 6), commissural EPSPs in VIP neurons were small (1.52 mV ± 1.08 mV) and had moderate 10 – 90% rise times (8.3 ms ± 4.3 ms), halfwidths (19.6 ms ± 7.6 ms) and decay time constants (43.5 ms ± 16.8 ms) (**Figure 7F**). Adding the NMDA receptor antagonist D-AP5 to the bath significantly reduced the halfwidth of EPSPs (14.3 ms ± 4.7 ms, p = 0.006) and revealed a trend toward reducing the rise time (6.3 ms ± 1.6 ms, p = 0.09) and decay time constant (30.6 ms ± 7.3 ms, p = 0.06) of EPSPs (ANOVA for repeated measurements with Tukey post-hoc test). The remainder of the EPSP was completely blocked by the AMPA receptor antagonist NBQX (**Figure 7F**). These results suggest that VIP neurons in the ICc receive excitatory commissural input and express both AMPA and NMDA receptors at excitatory commissural synapses. Interestingly, commissural input activated NMDA receptors even though there was 1 mM $Mg^{2+}$ in the bath and the somatic membrane potential was at or near the resting membrane potential throughout the recording. This may indicate that commissural synapses are located on the distal dendrites and/or the dendritic spines of VIP neurons.

Combined, the commissural CRACM experiments show that VIP neurons in the ICc receive excitatory and inhibitory synaptic input from the contralateral IC. Surprisingly, although GABAergic neurons make up <= 20% of commissural projections (Hernández et al., 2006; Nakamoto et al., 2013), we found a higher connection probability for inhibitory commissural projections (6 out of 12 recordings, 50%) than for excitatory connections (11 out of 27 recordings, 29%).

## VIP neurons in the ICc receive synaptic input from the DCN

The DCN provides one of the major sources of excitatory input to the IC (Adams, 1979; Brunso-Bechtold et al., 1981; Oliver, 1984; Osen, 1972; Ryugo et al., 1981). A previous study has shown that DCN

afferents synapse onto glutamatergic and GABAergic neurons in the IC (Chen et al., 2018), but it is not known which specific classes of IC neurons receive input from the DCN. In addition, the physiology of DCN afferent synapses remains unknown. To test whether VIP neurons receive synaptic input from DCN principal neurons, we injected the right DCN with the AAV1.Syn.Chronos-GFP.WPRE.bGH viral vector and recorded from VIP neurons in the contralateral (left) ICc (**Figure 8A, left**). To confirm selective transfection of the DCN, we sliced the brainstem of every animal used and determined whether GFP expression was present and limited to the right DCN. If there was no transfection or if there was considerable expression of GFP in the auditory nerve or VCN, no recordings were performed. In most cases, GFP expression was limited to the DCN (**Figure 8A, right**) and GFP-labeled axons were present in the left ICc.

To block spontaneous IPSPs, we performed DCN CRACM experiments with GABAergic and glycinergic blockers in the bath (5 µm gabazine and 1 µM strychnine, **Figure 8B**). We found that 2 – 5 ms pulses of blue light elicited EPSPs in 19 of 25 neurons tested, confirming that ICc VIP neurons receive synaptic input from the DCN. Light-evoked EPSPs had moderate amplitudes (2.85 mV ± 2.98 mV) and relatively slow rise times (4.2 ms ± 1.3 ms), halfwidths (20.6 ms ± 14.4 ms) and decay time constants (22.0 ms ± 6.7 ms) (n = 6 cells, **Figure 8B, left and 8C**). Because EPSP kinetics were relatively slow, we hypothesized that DCN synapses activate NMDA receptors on VIP neurons. Interestingly, D-AP5 had no significant effect on any of the measured properties (amplitude: 2.80 mV ± 2.54 mV, $p = 0.96$, rise time: 4.4 ms ± 1.7 ms, $p = 0.95$, halfwidth: 15.4 ms ± 6.1 ms, $p = 0.37$, decay time constant: 29.0 ms ± 7.1 ms, $p = 0.16$, ANOVA for repeated measurements with Tukey post-hoc test) (**Figure 8B, middle, and 8C**). In contrast to commissural inputs where D-AP5 had a significant effect on EPSP kinetics, this suggests that DCN inputs to ICc VIP neurons do not activate NMDA receptors under resting conditions. Subsequent addition of NBQX completely abolished DCN-evoked EPSPs (**Figure 8B, right**), confirming that DCN synapses activate AMPA receptors on ICc VIP neurons.

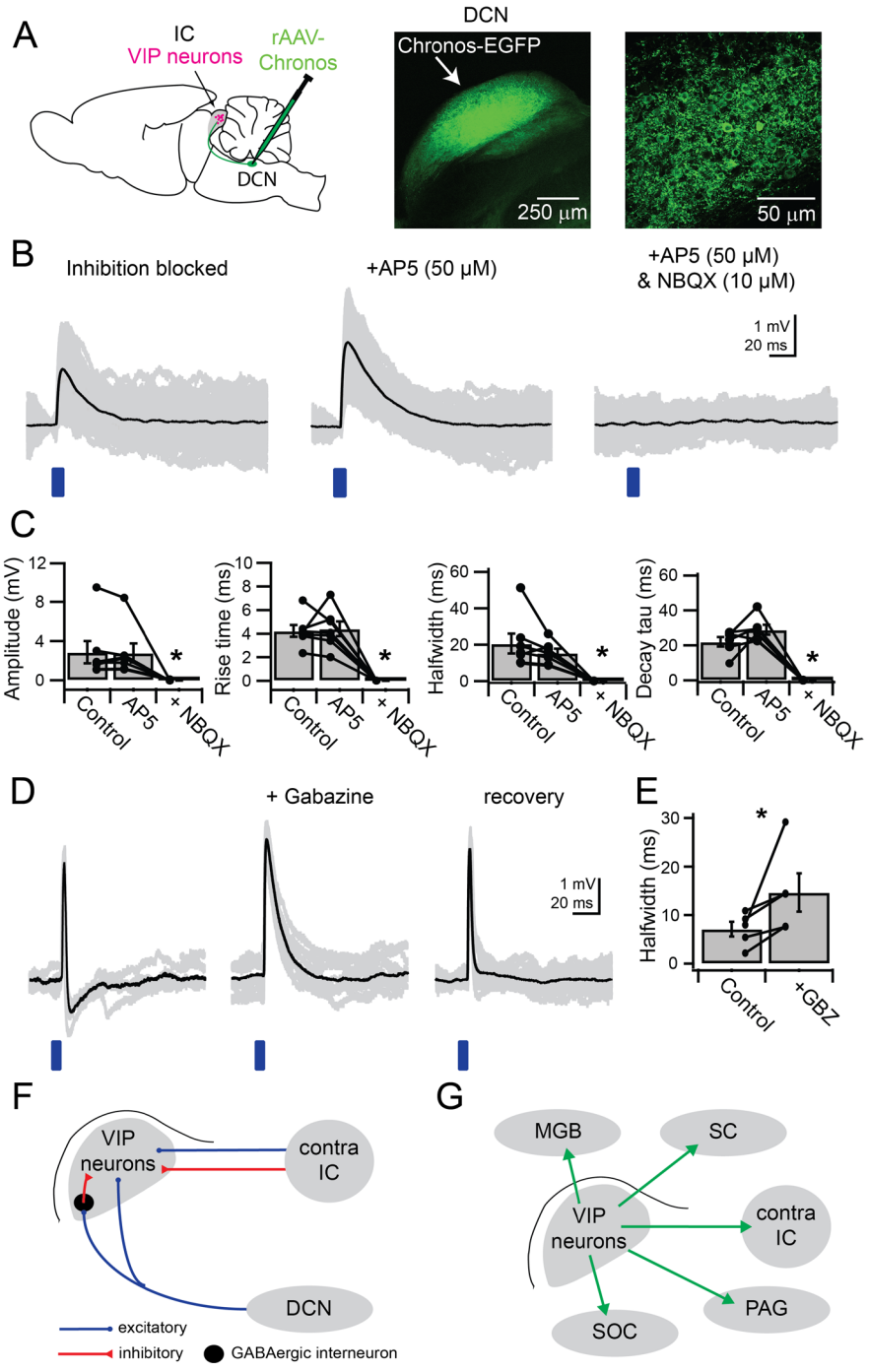


298

299 Given that fusiform cells in the DCN often fire at rates exceeding 100 Hz (Davis et al., 1996; Ma

300 and Brenowitz, 2012; Nelken and Young, 1994; Spirou and Young, 1991; Young and Brownell, 1976), the

301 slow kinetics of DCN-evoked EPSPs suggests that these EPSPs undergo temporal summation in VIP

302 neurons. Together, these results identify VIP neurons in the ICc as a distinct postsynaptic target of DCN

**Figure 8. VIP neurons in the ICc receive direct synaptic input from the DCN and feedforward inhibition driven by DCN afferents. (A)** Experimental setup. An AAV encoding Chronos-GFP was injected into the right DCN. For every experiment, the injection site and Chronos-GFP expression were confirmed through GFP fluorescence. Current clamp recordings were made from VIP neurons in the ICc contralateral to the injection site. **(B)** With inhibition blocked by gabazine and strychnine, 2 – 5 ms blue light flashes evoked EPSPs (left). AP5 did not significantly reduce EPSP halfwidth or decay time constant. Subsequent addition of NBQX abolished the EPSP. **(C)** Population data showing amplitude and kinetics for EPSPs elicited by activation of DCN synapses onto VIP neurons in the ICc. The absence of a significant effect of AP5 indicates that NMDA receptors did not make a significant contribution to EPSPs. **(D)** In several recordings made in the absence of inhibitory blockers, EPSP duration was limited through GABAergic feedforward inhibition (left; n = 5). In these instances, gabazine wash-in increased EPSP halfwidth to values similar to those in (B). **(E)** Population data for feedforward inhibition to VIP neurons. Washing in gabazine increased EPSP halfwidth in 5 out of 5 tested connections. **(F)** Summary of the sources of input to VIP neurons identified by CRACM experiments. **(G)** Summary of the major projection targets of VIP neurons identified by axonal tract tracing: MGB (medial geniculate body), SC (superior colliculus), contralateral IC, PAG (periaqueductal gray), SOC (superior olivary complex).

afferents. Given the number of conditions that must be met for a long-range CRACM experiment to succeed, our observation that the connection probability for DCN to VIP projections was 76% (19 of 25 neurons) suggests that most VIP neurons in the ICc receive input from the DCN.

## DCN afferents drive local feedforward inhibition onto VIP neurons in the ICc

We next repeated the DCN-CRACM experiments without $GABA_A$ and glycine receptor antagonists in the bath. Under these conditions, we observed that an IPSP was elicited 2 – 3 ms after the onset of the light-evoked EPSP (**Figure 8D**). This IPSP could vary in strength between recorded VIP neurons. In some instances, the IPSP slightly altered the halfwidth and decay time constant of the EPSP. In other cases, the IPSP strongly limited the EPSP duration and generated a hyperpolarization after the EPSP (**Figure 8D, left**). Washing in gabazine restored the EPSP to values comparable to the EPSPs recorded in the presence of inhibitory receptor antagonists (compare **Figure 8B, C**). Washing out gabazine restored the IPSP and limited EPSP halfwidth again (**Figure 8D, right**). Across five ICc VIP neurons, the IPSP significantly shortened the halfwidth of the elicited EPSP ($p = 0.048$, paired t-test, **Figure 8E**). Halfwidth reductions ranged from 22% to 73%, with a median reduction of 36%. Because DCN to IC projections are glutamatergic (Ito and Oliver, 2010; Oliver, 1984), and the periolivary nuclei and nuclei of the lateral lemniscus, the sources of ascending GABAergic input to the IC (González-Hernández et al., 1996), were

not present in the brain slice, this inhibition must be due to DCN afferents activating a local feedforward inhibitory circuit within the IC. The latency to the IPSP onset also supports the theory of a disynaptic, local inhibitory circuit, as the IPSP always succeeded the initial EPSP. Thus, these results indicate that ascending input from the DCN activates a feedforward inhibitory circuit within the IC and that this circuit regulates the duration of DCN-evoked excitation in ICc VIP neurons.

## Discussion

By combining molecular genetics with physiological and anatomical approaches, we identified VIP neurons as a novel class of glutamatergic principal neurons in the auditory midbrain. In contrast to the diverse properties present in the broader population of IC neurons, VIP neurons consistently exhibited sustained firing patterns, spiny dendrites, and stellate morphology. Surprisingly, the identification of VIP neurons revealed that a molecularly-defined class of IC neurons can broadcast the output of the IC to multiple auditory and non-auditory brain regions. The identification of VIP neurons also enabled us to identify microcircuit motifs within the IC. In particular, we found that VIP neurons receive ascending input from the contralateral DCN and commissural input from the contralateral IC. Input from the DCN also drove feedforward inhibition that could sculpt the effects of excitatory inputs to VIP neurons. Thus, feedforward inhibitory circuits within the IC may regulate the temporal summation of ascending inputs. By integrating multiple sources of input and participating in most of the major projections from the IC, VIP neurons are well-positioned to broadly influence auditory computations in numerous brain regions.

### VIP neurons are a distinct class of IC neurons

It has long been argued that the classification of neurons requires a multifaceted analysis of morphological and physiological features (Tyner, 1975). More recent efforts have emphasized the importance of combining these features with molecular markers (Petilla Interneuron Nomenclature Group et al., 2008; Tremblay et al., 2016; Zeng and Sanes, 2017). This combination has proven to be particularly effective for unambiguously classifying neuron types. In the cerebral cortex, a multifaceted classification scheme including molecular markers has enabled investigations into how specific classes of interneurons shape circuit computations, sensory processing, and animal behavior (Cichon et al., 2017; Kato et al., 2017, 2015; Kuchibhotla et al., 2017; Lee et al., 2013; Milstein et al., 2015; Pfeffer et al., 2013; Pi et al., 2013). Similar approaches have succeeded in the amygdala, hypothalamus, basal ganglia,

and other brain regions where it was previously difficult to identify neuron types (Campbell et al., 2017; Capogna, 2014; Wallace et al., 2017).

In the auditory midbrain, previous efforts to identify neuron classes relied on in vitro physiology, in vivo physiology, morphology, neurochemical markers, or some combination of these (Beebe et al., 2016; Fujimoto et al., 2017; Malmierca et al., 1993; Oliver and Morest, 1984; Ono et al., 2005; Palmer et al., 2013; Peruzzi et al., 2000; Ramachandran et al., 1999; Schofield and Beebe, 2018; Sivaramakrishnan and Oliver, 2001). Despite these and other attempts, the only neuron class that has been consistently identified in the IC are the large GABAergic neurons (Beebe et al., 2016; Geis and Borst, 2013; Ito et al., 2015, 2009; Ito and Oliver, 2014). However, there are currently no known molecular markers for large GABAergic neurons, making it difficult to test the role of these neurons in auditory computations (Schofield and Beebe, 2018).

Using a multifaceted approach, we identified VIP neurons as a novel class of IC neurons. VIP neurons share a common set of molecular, neurochemical, morphological, and physiological features. VIP neurons are labeled in the VIP-IRES-Cre mouse line and are glutamatergic. Ninety-three percent of the ICc VIP neurons in our data set had a stellate morphology and 94% of all IC VIP neurons had dendritic spines. Similarly, 90% of VIP neurons had sustained firing patterns. Although the input resistance, membrane time constant, and expression of $I_h$ varied within the population of VIP neurons, for VIP neurons in the ICc, we found that a portion of this variability reflected their location along the tonotopic axis of the ICc.

It is important to note that it would not be possible to identify VIP neurons based on their morphology or physiology alone. VIP neurons are not the only stellate neurons in the IC, nor are they the only neurons with sustained firing patterns or dendritic spines. These results provide insight to why

it has been difficult to classify neuron types in the IC. We propose that a multidimensional approach incorporating molecular markers will be essential to identifying the remaining neuron classes in the IC.

**Diverse projection patterns of VIP neurons**

We found that VIP neurons project not only to MGB and contralateral IC, the most common recipients of IC projections, but also to the nucleus of the brachium of the IC, superior colliculus, periaqueductal gray, superior olivary complex, and ipsilateral IC (**Figure 6**). The number of extrinsic targets reached by VIP axons was a surprise given the relatively small population of VIP neurons. Do individual VIP neurons project to multiple targets? Previous retrograde labeling studies suggest that some patterns of collateral projection are more common than others for IC cells. IC cells that project to the contralateral thalamus appear to quite commonly have a collateral projection to the ipsilateral thalamus (Mellott et al., 2018). In contrast, very few IC neurons project to the thalamus and the cochlear nucleus (Coomes and Schofield, 2004; Hashikawa and Kawamura, 1983; Okoyama et al., 2006), or to the left and right cochlear nuclei (Schofield, 2001). Whether IC commissural cells can have collateral projections to the thalamus has been supported (González-Hernández et al., 1996) or denied (Okoyama et al., 2006). Because retrograde tracing studies underestimate collateral projections (Schofield et al., 2007), such studies may have missed VIP neurons with collateral projections.

Alternatively, individual VIP neurons might project to one or a few targets. It would then be possible to subdivide VIP neurons based on their axonal projections. This would parallel the cerebral cortex, where the major classes of interneurons contain subclasses that often differ in their axonal targeting (Tremblay et al., 2016). If such is the case, then the unifying feature of VIP neurons might be that they perform similar computational roles within circuits, even when the circuits themselves are involved in different functions. In any event, the axonal projection patterns of individual VIP neurons, to

391 extrinsic targets and within the IC, will be important features for further characterizing VIP subclasses
392 and their functional roles.

393 **Integration of synaptic input by VIP neurons**

394 Our results show that VIP neurons receive input from at least four sources: principal neurons in the DCN,
395 local inhibitory neurons, and excitatory and inhibitory neurons in the contralateral IC (**Figure 8G**). In
396 multiple instances, we observed that VIP neurons received input from the DCN and a local inhibitory
397 neuron or a combination of excitatory and inhibitory commissural input. Given that optogenetic circuit
398 mapping experiments underestimate connection probabilities (not all synapses are transfected by the
399 virus), these results suggest that many individual VIP neurons integrate input from ascending, local, and
400 commissural sources. In future studies, it will be important to determine whether VIP neurons receive
401 additional sources of synaptic input, as previous studies have shown that individual IC neurons can
402 integrate input from numerous sources (Ito et al., 2015; Ito and Oliver, 2014).

403 Excitatory postsynaptic responses in IC neurons often involve activation of NMDA receptors (Ma
404 et al., 2002; Wu et al., 2004). Under in vivo conditions, the activation of NMDA receptors can influence
405 how IC neurons respond to tones (Sanchez et al., 2007). In VIP neurons, we found that excitatory
406 commissural synapses activated AMPA and NMDA receptors, while synaptic input from DCN afferents
407 activated only AMPA receptors. The activation of NMDA receptors occurred even though our ACSF
408 contained 1 mM $Mg^{2+}$ and neurons were at their resting membrane potential. Interestingly, previous
409 studies have shown that NMDA receptors in some IC neurons can be activated under similar conditions,
410 even when AMPA are receptors blocked (Ma et al., 2002; Sivaramakrishnan and Oliver, 2006). The
411 activation of NMDA receptors in our recordings may indicate that excitatory commissural synapses tend
412 to be located on the distal dendrites or dendritic spines of VIP neurons, where the local membrane
413 potential might be sufficiently depolarized by activation of AMPA receptors to remove $Mg^{2+}$ block of

NMDA receptors. A distal location would be consistent with the proposed modulatory role for commissural inputs (Orton et al., 2016; Orton and Rees, 2014). Similarly, the lack of NMDA receptor activation by DCN afferents might indicate that DCN synapses are located proximal to the soma, possibly on the soma itself, or that these synapses lack NMDA receptors. These synaptic arrangements may have important implications for auditory coding and synaptic plasticity mechanisms in VIP neurons.

In many brain regions, feedforward inhibitory circuits control the time window for temporal integration of synaptic input (Gabernet et al., 2005; Pouille and Scanziani, 2001; Roberts et al., 2013; Stokes and Isaacson, 2010). In the ICc, it was recently shown that GABAergic neurons provide local inhibitory input mainly to neurons in the same isofrequency lamina (Sturm et al., 2014). However, the conditions that recruit local inhibition have remained unclear. Our data provide direct evidence that activation of DCN afferents can elicit both direct excitatory input and disynaptic feedforward inhibition to VIP neurons. Feedforward inhibition can dramatically reduce EPSP halfwidth, suggesting that local feedforward inhibition regulates the temporal summation of synaptic inputs. In addition, while DCN afferents elicited modest EPSPs in VIP neurons, DCN input presumably drove spiking in the GABAergic neurons that provided feedforward inhibition. It will be important for future studies to identify this population of GABAergic neurons and the extent of their influence on auditory computations in VIP and other IC neurons.

## Material and Methods

### *Animals*

All experiments were approved by the University of Michigan Institutional Animal Care and Use Committee and were in accordance with NIH guidelines for the care and use of laboratory animals. Animals were kept on a 12 hour day/night cycle with ad libitum access to food and water. VIP-IRES-Cre mice (*Vip*$^{tm1(cre)Zjh}$/J, Jackson Laboratory, stock # 010908)(Taniguchi et al., 2011) were crossed with Ai14 reporter mice (B6.Cg-*Gt(ROSA)26Sor*$^{tm14(CAG-tdTomato)Hze}$/J, Jackson Laboratory, stock # 007914)(Madisen et al., 2010) to yield F1 offspring that expressed the fluorescent protein tdTomato in VIP neurons. For control experiments, C57BL/6J mice (Jackson Laboratory, stock # 000664) were used.

### *Immunohistochemistry*

Mice were deeply anesthetized and perfused transcardially with 0.1 M phosphate-buffered saline (PBS), pH 7.4, for 1 min and then with a 10% buffered formalin solution (Millipore Sigma, cat# HT501128) for 10 min. Brains were collected and post-fixed in the same fixative for 2 hours and cryoprotected overnight at 4 °C in 0.1 M PBS containing 20% sucrose. Brains were cut into 40 µm sections on a vibratome or freezing microtome. Sections were rinsed in 0.1 M PBS, and then treated with 10% normal donkey serum (Jackson ImmunoResearch Laboratories, West Grove, PA) and 0.3% Triton X-100 for 2 hours. Slides were incubated overnight at 4 °C in mouse anti-GAD67 (1:1000; Millipore Sigma, cat# MAB5406), rabbit anti-NeuN (1:500; Millipore Sigma, cat# ABN78), or rabbit anti-bNOS (1:1000; Millipore Sigma, cat# N2280). The next day, sections were rinsed in 0.1 M PBS and incubated in Alexa Fluor 488-tagged donkey anti-mouse IgG or donkey anti-rabbit IgG (1:500, Thermo Fisher, cat# A-21202 and A-21206) for 1 hour at room temperature. Sections were then mounted on gelatin-subbed slides (SouthernBiotech, cat# SLD01-BX) and coverslipped using Fluoromount-G (SouthernBiotech, cat# 0100-

454 01). Images were collected using a 1.30 NA 40x oil-immersion objective or a 1.40 NA 63x oil-immersion
455 objective on a Leica TCS SP8 laser scanning confocal microscope.

456

457 *Antibody validation*

458 The mouse monoclonal anti-GAD67 antibody (Millipore Sigma, cat# MAB5406) was raised against the 67
459 kDA isoform of glutamic acid decarboxylase (GAD). The manufacturer reports that Western blot analysis
460 shows no cross-reactivity with the 65 kDa isoform of GAD (GAD65). This antibody has been previously
461 used to identify GABAergic cells in the IC (Beebe et al., 2016; Ito et al., 2009; Mellott et al., 2014). The
462 mouse monoclonal anti-nitric oxide synthase-brain (bNOS) (Sigma, cat# N2280) was raised against the
463 IgG1 isotype from the NOS-B1 hybridoma. The manufacturer reports that anti-bNOS reacts specifically
464 with nitric oxide synthase (NOS), derived from brain (bNOS, 150-160 kDa). This antibody has been
465 previously used, in guinea pig, to delineate the borders of the IC (Coote and Rees, 2008). To perform
466 NeuN staining, we used a rabbit polyclonal antibody (Millipore Sigma, cat# ABN78). The manufacturer
467 reports that anti-NeuN specifically recognizes the DNA-binding, neuron-specific protein NeuN, which is
468 present in most central and peripheral neuronal cell types of all vertebrates tested. Previous studies
469 reported the use of this antibody to label neurons in the IC (Beebe et al., 2016; Foster et al., 2014;
470 Mellott et al., 2014).

471

472 *Analysis of GAD67 staining*

473 Images from representative sections of the IC (n = 3 animals, 2 sections per animal, one caudal and one
474 middle) were collected at 2 µm depth intervals with a 1.30 NA 40x oil-immersion objective on a Leica
475 TCS SP8 laser scanning confocal microscope. Images were analyzed using Fiji software (Rueden et al.,
476 2017; Schindelin et al., 2012). Consistent with previous studies, we found that the anti-GAD67 antibody

did not penetrate the entire depth of the tissue sections (Beebe et al., 2016; Mellott et al., 2014). We therefore restricted our analysis to the top 10 – 12 µm of each section, where the antibody was fully penetrant. Within this region, we manually marked every GAD67$^+$ cell body and every tdTomato$^+$ cell body in the left IC. The green (GAD67) and red (tdTomato) color channels were analyzed separately, so that labeling in one channel did not influence analysis of the other channel. After cells were marked, the GAD67 and tdTomato color channels were merged, and every instance where a cell body contained markers for both GAD67 and tdTomato was counted. The number of double-labeled cells was compared to the total number of tdTomato$^+$ neurons to determine the percentage of tdTomato$^+$ neurons that were GAD67$^+$.

*Analysis of NeuN staining with design-based stereology*

A design-based stereology approach was used to estimate the numbers of NeuN$^+$ and tdTomato$^+$ neurons in anti-NeuN stained sections (Schmitz and Hof, 2005). To collect systematic random samples, a virtual 370 µm x 370 µm grid was overlaid on the IC section. The starting coordinates for the grid were set using the Mersenne Twister random number generator in Igor Pro 7 or 8 (WaveMetrics Inc.). Images were then collected at coordinates determined by the upper-left intersection of each grid-square that fell over the left IC. Each image consisted of a 184 µm x 184 µm Z-stack collected at 1 µm depth intervals with a 1.40 NA 63x oil immersion objective on a Leica TCS SP8 confocal microscope. Six to sixteen images were collected per slice. Three slices were analyzed per mouse, with slices from each mouse evenly distributed along the rostral-caudal axis of the IC. Images were imported to Neurolucida 360 (MBF Bioscience), where neurons were counted using the optical fractionator approach (West et al., 1991). In this approach, we determined the image planes corresponding to the top, center, and bottom of the slice in each image stack. Top and bottom regions of each slice (≥ 2 µm thick) were treated as guard zones and discarded from subsequent analysis. Removal of guard zones left a 15 µm-thick region at the

center of the slice for subsequent analysis. Neurons within this region were counted by making a single mark at the top of each cell. Cells crossing the right and top borders of the image stack were counted, whereas those crossing the left and bottom borders were not. The green (NeuN) and red (tdTomato) color channels were analyzed separately, so that labeling in one channel did not affect analysis of the other. Next, the color channels were merged and cells with both NeuN and tdTomato markers were counted. In every instance, tdTomato$^+$ cells were also NeuN$^+$ (205/205 cells). The total number of double-labeled (tdTomato$^+$/NeuN$^+$) cells was then compared to the total number of NeuN$^+$ cells.

*Analysis of the distribution of VIP neurons*

Following transcardial perfusion as described previously, brains from three VIP-IRES-Cre x Ai14 mice were frozen and sectioned on a sliding microtome. Brains were cut into 40 µm sections, one each in the transverse, sagittal, and horizontal planes, and sections were collected in three series. The distribution of tdTomato-expressing (VIP$^+$) cells in one series from each case was analyzed using a Neurolucida system (MBF Bioscience, Williston, VT) attached to a Zeiss Axioimager.Z1 fluorescence microscope. Major IC subdivisions, including the central nucleus (ICc), dorsal cortex, (ICd) and lateral cortex (IClc), were identified by comparing bNOS and GAD67 immunostains with previous studies of mouse IC (Willard and Ryugo, 1983; Meininger et al., 1986; Ono et al., 2016; Dillingham et al., 2017). Neurolucida Explorer was used to export drawings to Adobe Illustrator for figure preparation.

*Electrophysiology*

Mice of either sex were used, aged postnatal day (P) 21 to P70 for VIP-IRES-Cre x Ai14 crosses and P21 to P113 for C57BL/6J animals. Mice were deeply anesthetized with isoflurane, decapitated, and the brain was dissected quickly in ~34° C artificial cerebrospinal fluid (ACSF) containing (in mM): 125 NaCl,

524 12.5 Glucose, 25 $NaHCO_3$, 3 KCl, 1.25 $NaH_2PO_4$, 1.5 $CaCl_2$, 1 $MgSO_4$, bubbled to a pH of 7.4 with 5% $CO_2$ in
525 95% $O_2$. Chemicals were obtained from Fisher Scientific or Millipore Sigma unless stated otherwise.
526 Coronal or parasagittal slices (200 – 250 µm) containing the IC were cut with a vibrating microtome
527 (VT1200S, Leica Biosystems) and incubated at 34 °C for 30 minutes in a holding chamber filled with ACSF
528 and bubbled with 5% $CO_2$ in 95% $O_2$. After incubation, slices were stored at room temperature until used
529 for recordings.

530 To make recordings, slices were placed in a recording chamber under a fixed stage upright
531 microscope (BX51WI, Olympus Life Sciences) and were constantly perfused with 34 °C ACSF at ~2
532 ml/min. All recordings were conducted near physiological temperature (34 °C). IC neurons were patched
533 under visual control using infrared Dodt gradient contrast and epifluorescence imaging. Recordings were
534 performed with a BVC-700A patch clamp amplifier (Dagan Corporation). Data were low pass filtered at
535 10 kHz, sampled at 50 kHz with a National Instruments PCIe-6343 data acquisition board, and acquired
536 using custom written algorithms in Igor Pro. For every recording, series resistance and pipette
537 capacitance were corrected using the bridge balance circuitry of the BVC-700A. Recordings with a series
538 resistance above 25 MΩ were discarded. All membrane potentials have been corrected for a liquid
539 junction potential of 11 mV.

540 Electrodes were pulled from borosilicate glass (outer diameter 1.5 mm, inner diameter 0.86
541 mm, Sutter Instrument) to a resistance of 3.5 – 4.5 MΩ using a P-1000 microelectrode puller (Sutter
542 Instrument). The electrode internal solution contained (in mM): 115 K-gluconate, 7.73 KCl, 0.5 EGTA, 10
543 HEPES, 10 $Na_2$ phosphocreatine, 4 MgATP, 0.3 NaGTP, supplemented with 0.1% biocytin (w/v), pH
544 adjusted to 7.3 with KOH and osmolality to 290 mmol/kg with sucrose.

545 Input resistance was determined by delivering a series of 100 ms hyperpolarizing current steps
546 incremented to elicit hyperpolarization ranging from just below the resting membrane potential to

547 < -110 mV. For each response, the amplitudes of the peak (most negative value) and steady-state
548 (average of last 10 ms of response) hyperpolarization were measured relative to the resting potential.
549 Voltage versus current plots were prepared, and input resistance was determined from the slopes of
550 lines fit to the peak ($R_{pk}$) and steady-state ($R_{ss}$) data for current steps that achieved a peak
551 hyperpolarization between 0 and -15 mV relative to rest. Membrane time constant was determined by
552 delivering 50 current steps at an amplitude that hyperpolarized the membrane potential by 1 – 3 mV.
553 Current step duration was set to ensure that the membrane potential achieved a steady-state value
554 before the end of the current step. An exponential function was then fit to onset of each response and
555 the median time constant determined.

556 To isolate or manipulate synaptic events, the following pharmacological agents were used, all
557 diluted in standard ACSF: 5 µM SR95531 (gabazine, $GABA_A$ receptor antagonist, Hello Bio), 1 µM
558 strychnine hydrochloride (glycine receptor antagonist, Millipore Sigma), 50 µM D-AP5 (NMDA receptor
559 antagonist, Hello Bio), 10 µM NBQX disodium salt (AMPA receptor antagonist, Hello Bio).

560 Data analysis was performed using custom written algorithms in Igor Pro or MATLAB (Mathworks).
561 Statistical tests were performed in R Studio (RStudio, Boston) for R 3.5.1 (The R Project for Statistical
562 Computing, The R Foundation).

563

564 *Post-hoc reconstructions of morphology and morphology analysis*
565 After recordings, the electrode was removed slowly to allow the cell membrane to reseal, and the slice
566 was fixed in 4% paraformaldehyde (PFA) in 0.1 M phosphate buffer (PB, pH 7.4) for 12 – 24 hours. Slices
567 were then washed in 0.1 M PB and stored in 0.1 M PB for up to three weeks. Recorded neurons were
568 stained using fluorescent biocytin-streptavidin histochemistry. In brief, slices were washed in 0.1 M PB
569 three times for 10 minutes (3 x 10 min in PB), permeabilized in 0.2% Triton X-100 in 0.1 M PB for 2

hours, washed 3 x 10 min in PB, and stained at 4 °C for 48 hours with streptavidin-Alexa Fluor 488 or 647, diluted 1:1000 in 0.1 M PB. Slices were then washed 3 x 10 min in PB and mounted on Superfrost Plus microscope slides in anti-fade media (Fluoromount-G). Z-stack images of streptavidin-Alexa Fluor labeled cells were obtained with a Leica TCS SP8 laser scanning confocal microscope using a 1.40 NA 63x oil-immersion objective. Three-dimensional reconstructions of neuronal morphology and quantitative analyses of soma and dendrite shape were performed on image stacks imported into Neurolucida 360 (MBF Bioscience). To facilitate comparisons of neuronal morphology, all reconstructed neurons are displayed as if they were in the left IC as viewed from a caudal perspective. Reconstructions of neurons that were located in the right IC were flipped along the dorsal-ventral axis so that they appear as if they were in the left IC.

*Correlation of neuron location and intrinsic physiology*

Following biocytin-streptavidin histochemistry, tile scan images of the entire IC were collected using a 20x objective on a Leica TCS SP8 confocal microscope. These images were then used to determine medial-lateral and dorsal-ventral coordinates of recorded neurons. The medial-lateral coordinate was measured as the distance of the soma from the medial axis (midline) of the IC slice (x axis). The dorsal-ventral coordinate was measured as the distance of the soma from the dorsal-most edge of the IC slice (y axis). Neurons in the right IC were combined with those from the left IC by multiplying the medial-lateral coordinate of neurons from the right IC by -1. Neuron coordinates were then compared to physiological parameters obtained during whole cell recordings. To test for correlations, data were fit with a plane using the Levenberg-Marquardt least squares method in Igor Pro. Fit quality was assessed with Pearson's correlation coefficient and the adjusted $R^2$. Fit significance (p value) was calculated based on the chi-squared statistic from the fit and the chi-squared cumulative distribution function.

*Determination of major axes of neuron morphology*

Neuron morphology was reconstructed as described above. To determine the "length" and "width" axes of the dendritic arbors, the set of coordinates describing the morphology of the dendritic arbor of each neuron was exported from Neurolucida 360 (MBF Bioscience). Coordinates were imported to Igor Pro, where principal components analysis (PCA) was performed on either the x and y coordinates (2D PCA) or the x, y, and z coordinates (3D PCA). The orientation of the length and width axes was then derived from the first and second principal directions of the resulting eigenvector matrices. 2D PCA was used to determine the orientation of neurons within the coronal plane. 3D PCA was used to determine the axes to use for measuring dendritic arbor length/width ratios. For this, the spread of the dendritic arbor along the first and second principal directions was determined by rotating each morphology coordinate set according to its eigenvector matrix, then calculating the range from the minimum to maximum coordinates along the x (length, first principal direction) and y (width, second principal direction) axes.

*Intracranial virus injections*

Intracranial virus injections were performed on mice age P21 – P35 using standard aseptic techniques. Throughout the procedure, mice were anesthetized with isoflurane and their body temperature maintained with a homeothermic heating pad. An injection of the analgesic carprofen (5 mg/kg, CarproJect, Henry Schein Animal Health) was delivered subcutaneously. The scalp was shaved and a rostro-caudal incision was made along the midline to expose the skull. Injection sites were mapped using stereotaxic coordinates relative to the lambda suture. A single craniotomy was performed using a micromotor drill (K.1050, Foredom Electric Co.) with a 0.5 mm burr (Fine Science Tools).

Viral constructs were injected with a NanoJect III nanoliter injector (Drummond Scientific Company) connected to a MP-285 micromanipulator (Sutter Instruments). Glass injection pipettes were prepared by pulling capillary glass (Drummond Scientific Company) with a P-1000 microelectrode puller

**Table 3. Stereotaxic coordinates for virus injections.** All coordinates are relative to the lambda suture.

| Location | X coordinate (caudal) | Y coordinate (lateral) | Z coordinates (depth) |
|---|---|---|---|
| Right IC penetration 1 (CRACM) | -900 µm | 1000 µm | 2250-1500 µm, 250 µm interval |
| Right IC penetration 2 (CRACM) | -900 µm | 1250 µm | 2250-1750 µm, 250 µm interval |
| Right IC penetration 1 (axonal tracing) | -900 µm | 1000 µm | 1850 µm, 2000 µm |
| Right DCN | -1325 µm | 2150 µm | 4750 µm, 4550 µm |

(Sutter Instrument). The injector tip was cut to an opening of ~20 µm and beveled at 30° with a BV-10 pipette beveller (Sutter Instrument). Injectors were back-filled with mineral oil and then front-filled with virus. AAV1.Syn.Chronos-GFP.WPRE.bGH (University of Pennsylvania Vector Core, Lot# CS1027L, 2.986e13 genome copies (GC)/ml) was used for CRACM experiments. AAV1.CAG.FLEX.eGFP.WPRE.bGH (Allen Institute 854, University of Pennsylvania Vector Core, Lot# CS0922, 4.65e13 GC/ml) was used for axonal tract tracing. For CRACM experiments, the IC was injected via two penetrations. Virus deposits were made at 250 µm intervals along the dorsal-ventral axis, resulting in four deposits in penetration 1 and three deposits in penetration 2. At each depth, 20 nl of virus was deposited, resulting in seven virus deposits and a total load of 140 nl virus per injected IC. DCN injections were limited to two deposits of 20 nl virus. For axonal tracing studies, viral load was reduced to 40 nl total (20 nl per site) to achieve sparser labeling of neurons. Injections were made at the coordinates shown in **Table 3**.

After injections were completed, the scalp was sutured with Ethilon 6-0 (0.7 metric) nylon sutures (Ethicon USA LLC), and the wound was treated with 0.5 – 1 ml 2% Lidocaine hydrochloride jelly (Akorn Inc.). Once mice were ambulatory, they were returned to the vivarium where they were monitored daily until sutures fell out and the wound was completely healed.

634 *Channelrhodopsin-assisted circuit mapping*

635 After allowing 3 – 4 weeks for Chronos expression, animals were used for in vitro slice electrophysiology
636 experiments as described above, with the exception that after decapitation all steps were performed in
637 red light and recordings were conducted in darkness or red light to limit Chronos activation. For CRACM
638 experiments, recordings were targeted to VIP neurons only. During whole cell recordings, Chronos was
639 activated by brief pulses of 470 nm light emitted by a blue LED coupled to the epi-fluorescence port of
640 the microscope. Blue light flashes were 2 to 5 ms long and optical power density ranged from 6 – 48
641 $mW/mm^2$, using a minimal stimulation protocol. Recording sweeps with light flashes were repeated 20
642 to 50 times in 0.5 – 1 s intervals to obtain average PSP values. During experiments to investigate
643 receptor contribution to PSPs, drugs were washed in for at least 10 minutes before recording under the
644 new condition. For each receptor antagonist, 7 - 8 washout experiments were conducted. In each case,
645 drug effects reversed after washout (data not shown).

646

647 *Axonal projections*

648 The right IC of VIP-IRES-Cre x Ai14 mice was injected with AAV1.CAG.FLEX.eGFP.WPRE.bGH and
649 transcardially perfused 3 – 4 weeks later, as described above. Brains were frozen and sectioned at 40 µm
650 on a sliding microtome. For some brains, sections were collected serially, and for others, sections were
651 collected in three series. The brains were examined for eGFP-labeled axons and boutons, which were
652 interpreted as $VIP^+$ projections originating in the IC. Some sections were counterstained with a
653 fluorescent Nissl stain (Neurotrace 640/660, ThermoFisher, cat# N21483). Injection sites comprised a
654 collection of eGFP-labeled cell bodies. Cases were included for analysis only if the eGFP labeled cell
655 bodies were restricted to the IC. Images were collected on a Zeiss AxioImager.Z2 microscope. High
656 magnification images were collected as z-stacks using a 1.40 NA 63X oil-immersion objective and
657 structured illumination (Zeiss Apotome 2) for optical sectioning at 0.5 µm intervals. Images shown are

maximum projections of collected stacks. Adobe Photoshop was used to colorize images, to globally adjust levels, and to add scale bars.

660 **Acknowledgements:** We thank Gabriel Corfas and Carol F. Elias for helpful discussions and advice. This
661 work was supported by a Deutsche Forschungsgemeinschaft Research Fellowship (GO 3060/1-1, project
662 number 401540516, to DG), an Emerging Research Grant from the Hearing Health Foundation (MTR),
663 and National Institutes of Health Grants R56 DC016880 (MTR) and R01 DC004391 (BRS).

664 **Competing interests:** The authors declare they have no financial or non-financial competing interests.

665 **References**

666 Adams JC. 1979. Ascending projections to the inferior colliculus. *J Comp Neurol* **183**:519–538.
667 doi:10.1002/cne.901830305
668 Baumann VJ, Lehnert S, Leibold C, Koch U. 2013. Tonotopic organization of the hyperpolarization-
669 activated current (Ih) in the mammalian medial superior olive. *Front Neural Circuits* **7**:117.
670 doi:10.3389/fncir.2013.00117
671 Beebe NL, Young JW, Mellott JG, Schofield BR. 2016. Extracellular Molecular Markers and Soma Size of
672 Inhibitory Neurons: Evidence for Four Subtypes of GABAergic Cells in the Inferior Colliculus. *J*
673 *Neurosci Off J Soc Neurosci* **36**:3988–3999. doi:10.1523/JNEUROSCI.0217-16.2016
674 Brunso-Bechtold JK, Thompson GC, Masterton RB. 1981. HRP study of the organization of auditory
675 afferents ascending to central nucleus of inferior colliculus in cat. *J Comp Neurol* **197**:705–722.
676 doi:10.1002/cne.901970410
677 Calford MB, Aitkin LM. 1983. Ascending projections to the medial geniculate body of the cat: evidence
678 for multiple, parallel auditory pathways through thalamus. *J Neurosci* **3**:2365–2380.
679 doi:10.1523/JNEUROSCI.03-11-02365.1983
680 Campbell JN, Macosko EZ, Fenselau H, Pers TH, Lyubetskaya A, Tenen D, Goldman M, Verstegen AMJ,
681 Resch JM, McCarroll SA, Rosen ED, Lowell BB, Tsai LT. 2017. A molecular census of arcuate
682 hypothalamus and median eminence cell types. *Nat Neurosci* **20**:484–496. doi:10.1038/nn.4495
683 Capogna M. 2014. GABAergic cell type diversity in the basolateral amygdala. *Curr Opin Neurobiol*, SI:
684 Inhibition: Synapses, Neurons and Circuits **26**:110–116. doi:10.1016/j.conb.2014.01.006
685 Chen C, Cheng M, Ito T, Song S. 2018. Neuronal Organization in the Inferior Colliculus Revisited with Cell-
686 Type-Dependent Monosynaptic Tracing. *J Neurosci Off J Soc Neurosci* **38**:3318–3332.
687 doi:10.1523/JNEUROSCI.2173-17.2018
688 Cichon J, Blanck TJJ, Gan W-B, Yang G. 2017. Activation of cortical somatostatin interneurons prevents
689 the development of neuropathic pain. *Nat Neurosci* **20**:1122–1132. doi:10.1038/nn.4595
690 Coomes DL, Schofield BR. 2004. Separate projections from the inferior colliculus to the cochlear nucleus
691 and thalamus in guinea pigs. *Hear Res* **191**:67–78. doi:10.1016/j.heares.2004.01.009
692 Coote EJ, Rees A. 2008. The distribution of nitric oxide synthase in the inferior colliculus of guinea pig.
693 *Neuroscience* **154**:218–225. doi:10.1016/j.neuroscience.2008.02.030
694 Davis KA, Ding J, Benson TE, Voigt HF. 1996. Response properties of units in the dorsal cochlear nucleus
695 of unanesthetized decerebrate gerbil. *J Neurophysiol* **75**:1411–1431.
696 doi:10.1152/jn.1996.75.4.1411
697 Dillingham CH, Gay SM, Behrooz R, Gabriele ML. 2017. Modular-extramodular organization in
698 developing multisensory shell regions of the mouse inferior colliculus. *J Comp Neurol* **525**:3742–
699 3756. doi:10.1002/cne.24300
700 Felix RA, Gourévitch B, Portfors CV. 2018. Subcortical pathways: Towards a better understanding of
701 auditory disorders. *Hear Res* **362**:48–60. doi:10.1016/j.heares.2018.01.008
702 Foster NL, Mellott JG, Schofield BR. 2014. Perineuronal nets and GABAergic cells in the inferior colliculus
703 of guinea pigs. *Front Neuroanat* **7**:53. doi:10.3389/fnana.2013.00053
704 Fujimoto H, Konno K, Watanabe M, Jinno S. 2017. Late postnatal shifts of parvalbumin and nitric oxide
705 synthase expression within the GABAergic and glutamatergic phenotypes of inferior colliculus
706 neurons. *J Comp Neurol* **525**:868–884. doi:10.1002/cne.24104
707 Gabernet L, Jadhav SP, Feldman DE, Carandini M, Scanziani M. 2005. Somatosensory integration
708 controlled by dynamic thalamocortical feed-forward inhibition. *Neuron* **48**:315–327.
709 doi:10.1016/j.neuron.2005.09.022

Geis HRAP, Borst JGG. 2013. Large GABAergic neurons form a distinct subclass within the mouse dorsal cortex of the inferior colliculus with respect to intrinsic properties, synaptic inputs, sound responses, and projections. *J Comp Neurol* **521**:189–202. doi:10.1002/cne.23170

Glendenning KK, Masterton RB. 1983. Acoustic chiasm: efferent projections of the lateral superior olive. *J Neurosci* **3**:1521–1537. doi:10.1523/JNEUROSCI.03-08-01521.1983

González-Hernández T, Mantolán-Sarmiento B, González-González B, Pérez-González H. 1996. Sources of GABAergic input to the inferior colliculus of the rat. *J Comp Neurol* **372**:309–326. doi:10.1002/(SICI)1096-9861(19960819)372:2<309::AID-CNE11>3.0.CO;2-E

Hashikawa T, Kawamura K. 1983. Retrograde labeling of ascending and descending neurons in the inferior colliculus. A fluorescent double labelling study in the cat. *Exp Brain Res* **49**:457–461.

Hassfurth B, Magnusson AK, Grothe B, Koch U. 2009. Sensory deprivation regulates the development of the hyperpolarization-activated current in auditory brainstem neurons. *Eur J Neurosci* **30**:1227–1238. doi:10.1111/j.1460-9568.2009.06925.x

Hernández O, Rees A, Malmierca MS. 2006. A GABAergic component in the commissure of the inferior colliculus in rat. *Neuroreport* **17**:1611–1614. doi:10.1097/01.wnr.0000236857.70715.be

Herrera M, Correa J, Sanchez F del C, Ruiz A. 1988. Stellate cells and their axonal patterns in the central nucleus of the inferior colliculus of the cat (Felis domesticus). *J Hirnforsch* **29**:393–402.

Ito T, Bishop DC, Oliver DL. 2009. Two classes of GABAergic neurons in the inferior colliculus. *J Neurosci Off J Soc Neurosci* **29**:13860–13869. doi:10.1523/JNEUROSCI.3454-09.2009

Ito T, Hioki H, Sohn J, Okamoto S, Kaneko T, Iino S, Oliver DL. 2015. Convergence of lemniscal and local excitatory inputs on large GABAergic tectothalamic neurons. *J Comp Neurol*. doi:10.1002/cne.23789

Ito T, Oliver DL. 2014. Local and commissural IC neurons make axosomatic inputs on large GABAergic tectothalamic neurons. *J Comp Neurol* **522**:3539–3554. doi:10.1002/cne.23623

Ito T, Oliver DL. 2012. The basic circuit of the IC: tectothalamic neurons with different patterns of synaptic organization send different messages to the thalamus. *Front Neural Circuits* **6**:48. doi:10.3389/fncir.2012.00048

Ito T, Oliver DL. 2010. Origins of Glutamatergic Terminals in the Inferior Colliculus Identified by Retrograde Transport and Expression of VGLUT1 and VGLUT2 Genes. *Front Neuroanat* **4**:135. doi:10.3389/fnana.2010.00135

Kato HK, Asinof SK, Isaacson JS. 2017. Network-Level Control of Frequency Tuning in Auditory Cortex. *Neuron* **95**:412-423.e4. doi:10.1016/j.neuron.2017.06.019

Kato HK, Gillet SN, Isaacson JS. 2015. Flexible Sensory Representations in Auditory Cortex Driven by Behavioral Relevance. *Neuron* **88**:1027–1039. doi:10.1016/j.neuron.2015.10.024

Klapoetke NC, Murata Y, Kim SS, Pulver SR, Birdsey-Benson A, Cho YK, Morimoto TK, Chuong AS, Carpenter EJ, Tian Z, Wang J, Xie Y, Yan Z, Zhang Y, Chow BY, Surek B, Melkonian M, Jayaraman V, Constantine-Paton M, Wong GK-S, Boyden ES. 2014. Independent optical excitation of distinct neural populations. *Nat Methods* **11**:338–346. doi:10.1038/nmeth.2836

Kuchibhotla KV, Gill JV, Lindsay GW, Papadoyannis ES, Field RE, Sten TAH, Miller KD, Froemke RC. 2017. Parallel processing by cortical inhibition enables context-dependent behavior. *Nat Neurosci* **20**:62–71. doi:10.1038/nn.4436

Lee S, Kruglikov I, Huang ZJ, Fishell G, Rudy B. 2013. A disinhibitory circuit mediates motor integration in the somatosensory cortex. *Nat Neurosci* **16**:1662–1670. doi:10.1038/nn.3544

Ma CL, Kelly JB, Wu SH. 2002. AMPA and NMDA receptors mediate synaptic excitation in the rat's inferior colliculus. *Hear Res* **168**:25–34.

Ma W-LD, Brenowitz SD. 2012. Single-neuron recordings from unanesthetized mouse dorsal cochlear nucleus. *J Neurophysiol* **107**:824–835. doi:10.1152/jn.00427.2011

757 Madisen L, Zwingman TA, Sunkin SM, Oh SW, Zariwala HA, Gu H, Ng LL, Palmiter RD, Hawrylycz MJ,
758 Jones AR, Lein ES, Zeng H. 2010. A robust and high-throughput Cre reporting and
759 characterization system for the whole mouse brain. *Nat Neurosci* **13**:133–140.
760 doi:10.1038/nn.2467
761 Malmierca MS, Blackstad TW, Osen KK, Karagülle T, Molowny RL. 1993. The central nucleus of the
762 inferior colliculus in rat: a Golgi and computer reconstruction study of neuronal and laminar
763 structure. *J Comp Neurol* **333**:1–27. doi:10.1002/cne.903330102
764 Malmierca MS, Izquierdo MA, Cristaudo S, Hernández O, Pérez-González D, Covey E, Oliver DL. 2008. A
765 discontinuous tonotopic organization in the inferior colliculus of the rat. *J Neurosci Off J Soc*
766 *Neurosci* **28**:4767–4776. doi:10.1523/JNEUROSCI.0238-08.2008
767 Meininger V, Pol D, Derer P. 1986. The inferior colliculus of the mouse. A Nissl and Golgi study.
768 *Neuroscience* **17**:1159–1179.
769 Mellott JG, Beebe NL, Schofield BR. 2018. Bilateral projections to the thalamus from individual neurons
770 in the inferior colliculus. *J Comp Neurol*. [In press]
771 Mellott JG, Foster NL, Nakamoto KT, Motts SD, Schofield BR. 2014. Distribution of GABAergic cells in the
772 inferior colliculus that project to the thalamus. *Front Neuroanat* **8**:17.
773 doi:10.3389/fnana.2014.00017
774 Merchán M, Aguilar LA, Lopez-Poveda EA, Malmierca MS. 2005. The inferior colliculus of the rat:
775 quantitative immunocytochemical study of GABA and glycine. *Neuroscience* **136**:907–925.
776 doi:10.1016/j.neuroscience.2004.12.030
777 Milstein AD, Bloss EB, Apostolides PF, Vaidya SP, Dilly GA, Zemelman BV, Magee JC. 2015. Inhibitory
778 Gating of Input Comparison in the CA1 Microcircuit. *Neuron* **87**:1274–1289.
779 doi:10.1016/j.neuron.2015.08.025
780 Moore DR. 1988. Auditory brainstem of the ferret: sources of projections to the inferior colliculus. *J*
781 *Comp Neurol* **269**:342–354. doi:10.1002/cne.902690303
782 Nakamoto KT, Sowick CS, Schofield BR. 2013. Auditory cortical axons contact commissural cells
783 throughout the guinea pig inferior colliculus. *Hear Res* **306**:131–144.
784 doi:10.1016/j.heares.2013.10.003
785 Nelken I, Young ED. 1994. Two separate inhibitory mechanisms shape the responses of dorsal cochlear
786 nucleus type IV units to narrowband and wideband stimuli. *J Neurophysiol* **71**:2446–2462.
787 Okoyama S, Ohbayashi M, Ito M, Harada S. 2006. Neuronal organization of the rat inferior colliculus
788 participating in four major auditory pathways. *Hear Res* **218**:72–80.
789 doi:10.1016/j.heares.2006.04.004
790 Oliver DL. 1987. Projections to the inferior colliculus from the anteroventral cochlear nucleus in the cat:
791 Possible substrates for binaural interaction. *J Comp Neurol* **264**:24–46.
792 doi:10.1002/cne.902640104
793 Oliver DL. 1984. Dorsal cochlear nucleus projections to the inferior colliculus in the cat: A light and
794 electron microscopic study. *J Comp Neurol* **224**:155–172. doi:10.1002/cne.902240202
795 Oliver DL, Kuwada S, Yin TC, Haberly LB, Henkel CK. 1991. Dendritic and axonal morphology of HRP-
796 injected neurons in the inferior colliculus of the cat. *J Comp Neurol* **303**:75–100.
797 doi:10.1002/cne.903030108
798 Oliver DL, Morest DK. 1984. The central nucleus of the inferior colliculus in the cat. *J Comp Neurol*
799 **222**:237–264. doi:10.1002/cne.902220207
800 Oliver DL, Winer JA, Beckius GE, Saint Marie RL. 1994. Morphology of GABAergic neurons in the inferior
801 colliculus of the cat. *J Comp Neurol* **340**:27–42. doi:10.1002/cne.903400104
802 Ono M, Bishop DC, Oliver DL. 2017. Identified GABAergic and Glutamatergic Neurons in the Mouse
803 Inferior Colliculus Share Similar Response Properties. *J Neurosci* **37**:8952–8964.
804 doi:10.1523/JNEUROSCI.0745-17.2017

805 Ono M, Bishop DC, Oliver DL. 2016. Long-Lasting Sound-Evoked Afterdischarge in the Auditory Midbrain.
806 *Sci Rep* **6**:20757. doi:10.1038/srep20757
807 Ono M, Yanagawa Y, Koyano K. 2005. GABAergic neurons in inferior colliculus of the GAD67-GFP knock-
808 in mouse: electrophysiological and morphological properties. *Neurosci Res* **51**:475–492.
809 doi:10.1016/j.neures.2004.12.019
810 Orton LD, Papasavvas CA, Rees A. 2016. Commissural Gain Control Enhances the Midbrain
811 Representation of Sound Location. *J Neurosci Off J Soc Neurosci* **36**:4470–4481.
812 doi:10.1523/JNEUROSCI.3012-15.2016
813 Orton LD, Rees A. 2014. Intercollicular commissural connections refine the representation of sound
814 frequency and level in the auditory midbrain. *eLife* **3**. doi:10.7554/eLife.03764
815 Osen KK. 1972. Projection of the cochlear nuclei on the inferior colliculus in the cat. *J Comp Neurol*
816 **144**:355–372. doi:10.1002/cne.901440307
817 Palmer AR, Shackleton TM, Sumner CJ, Zobay O, Rees A. 2013. Classification of frequency response areas
818 in the inferior colliculus reveals continua not discrete classes. *J Physiol* **591**:4003–4025.
819 doi:10.1113/jphysiol.2013.255943
820 Paloff AM, Usunoff KG, Hinova-Palova DV. 1992. Ultrastructure of Golgi-impregnated and gold-toned
821 neurons in the central nucleus of the inferior colliculus in the cat. *J Hirnforsch* **33**:361–407.
822 Peruzzi D, Sivaramakrishnan S, Oliver DL. 2000. Identification of cell types in brain slices of the inferior
823 colliculus. *Neuroscience* **101**:403–416.
824 Petilla Interneuron Nomenclature Group, Ascoli GA, Alonso-Nanclares L, Anderson SA, Barrionuevo G,
825 Benavides-Piccione R, Burkhalter A, Buzsáki G, Cauli B, Defelipe J, Fairén A, Feldmeyer D, Fishell
826 G, Fregnac Y, Freund TF, Gardner D, Gardner EP, Goldberg JH, Helmstaedter M, Hestrin S,
827 Karube F, Kisvárday ZF, Lambolez B, Lewis DA, Marin O, Markram H, Muñoz A, Packer A,
828 Petersen CCH, Rockland KS, Rossier J, Rudy B, Somogyi P, Staiger JF, Tamas G, Thomson AM,
829 Toledo-Rodriguez M, Wang Y, West DC, Yuste R. 2008. Petilla terminology: nomenclature of
830 features of GABAergic interneurons of the cerebral cortex. *Nat Rev Neurosci* **9**:557–568.
831 doi:10.1038/nrn2402
832 Petreanu L, Huber D, Sobczyk A, Svoboda K. 2007. Channelrhodopsin-2-assisted circuit mapping of long-
833 range callosal projections. *Nat Neurosci* **10**:663–668. doi:10.1038/nn1891
834 Pfeffer CK, Xue M, He M, Huang ZJ, Scanziani M. 2013. Inhibition of inhibition in visual cortex: the logic
835 of connections between molecularly distinct interneurons. *Nat Neurosci* **16**:1068–1076.
836 doi:10.1038/nn.3446
837 Pi H-J, Hangya B, Kvitsiani D, Sanders JI, Huang ZJ, Kepecs A. 2013. Cortical interneurons that specialize in
838 disinhibitory control. *Nature* **503**:521–524. doi:10.1038/nature12676
839 Portfors CV, Mayko ZM, Jonson K, Cha GF, Roberts PD. 2011. Spatial organization of receptive fields in
840 the auditory midbrain of awake mouse. *Neuroscience* **193**:429–439.
841 doi:10.1016/j.neuroscience.2011.07.025
842 Pouille F, Scanziani M. 2001. Enforcement of temporal fidelity in pyramidal cells by somatic feed-
843 forward inhibition. *Science* **293**:1159–1163. doi:10.1126/science.1060342
844 Ramachandran R, Davis KA, May BJ. 1999. Single-unit responses in the inferior colliculus of decerebrate
845 cats. I. Classification based on frequency response maps. *J Neurophysiol* **82**:152–163.
846 Reetz G, Ehret G. 1999. Inputs from three brainstem sources to identified neurons of the mouse inferior
847 colliculus slice. *Brain Res* **816**:527–543.
848 Roberts MT, Seeman SC, Golding NL. 2013. A mechanistic understanding of the role of feedforward
849 inhibition in the mammalian sound localization circuitry. *Neuron* **78**:923–935.
850 doi:10.1016/j.neuron.2013.04.022

Rueden CT, Schindelin J, Hiner MC, DeZonia BE, Walter AE, Arena ET, Eliceiri KW. 2017. ImageJ2: ImageJ for the next generation of scientific image data. *BMC Bioinformatics* **18**:529. doi:10.1186/s12859-017-1934-z

Ryugo DK, Willard FH, Fekete DM. 1981. Differential afferent projections to the inferior colliculus from the cochlear nucleus in the albino mouse. *Brain Res* **210**:342–349.

Saint Marie RL. 1996. Glutamatergic connections of the auditory midbrain: selective uptake and axonal transport of D-[3H]aspartate. *J Comp Neurol* **373**:255–270. doi:10.1002/(SICI)1096-9861(19960916)373:2<255::AID-CNE8>3.0.CO;2-2

Sanchez JT, Gans D, Wenstrup JJ. 2007. Contribution of NMDA and AMPA receptors to temporal patterning of auditory responses in the inferior colliculus. *J Neurosci Off J Soc Neurosci* **27**:1954–1963. doi:10.1523/JNEUROSCI.2894-06.2007

Schindelin J, Arganda-Carreras I, Frise E, Kaynig V, Longair M, Pietzsch T, Preibisch S, Rueden C, Saalfeld S, Schmid B, Tinevez J-Y, White DJ, Hartenstein V, Eliceiri K, Tomancak P, Cardona A. 2012. Fiji: an open-source platform for biological-image analysis. *Nat Methods* **9**:676–682. doi:10.1038/nmeth.2019

Schmitz C, Hof PR. 2005. Design-based stereology in neuroscience. *Neuroscience* **130**:813–831. doi:10.1016/j.neuroscience.2004.08.050

Schofield BR. 2001. Origins of projections from the inferior colliculus to the cochlear nucleus in guinea pigs. *J Comp Neurol* **429**:206–220. doi:10.1002/1096-9861(20000108)429:2<206::AID-CNE3>3.0.CO;2-X

Schofield BR, Beebe NL. 2018. Subtypes of GABAergic cells in the inferior colliculus. *Hear Res*. doi:10.1016/j.heares.2018.10.001

Schofield BR, Schofield RM, Sorensen KA, Motts SD. 2007. On the use of retrograde tracers for identification of axon collaterals with multiple fluorescent retrograde tracers. *Neuroscience* **146**:773–783. doi:10.1016/j.neuroscience.2007.02.026

Sivaramakrishnan S, Oliver DL. 2006. Neuronal responses to lemniscal stimulation in laminar brain slices of the inferior colliculus. *J Assoc Res Otolaryngol JARO* **7**:1–14. doi:10.1007/s10162-005-0017-4

Sivaramakrishnan S, Oliver DL. 2001. Distinct K currents result in physiologically distinct cell types in the inferior colliculus of the rat. *J Neurosci Off J Soc Neurosci* **21**:2861–2877.

Spirou GA, Young ED. 1991. Organization of dorsal cochlear nucleus type IV unit response maps and their relationship to activation by bandlimited noise. *J Neurophysiol* **66**:1750–1768. doi:10.1152/jn.1991.66.5.1750

Stiebler I, Ehret G. 1985. Inferior colliculus of the house mouse. I. A quantitative study of tonotopic organization, frequency representation, and tone-threshold distribution. *J Comp Neurol* **238**:65–76. doi:10.1002/cne.902380106

Stokes CCA, Isaacson JS. 2010. From dendrite to soma: dynamic routing of inhibition by complementary interneuron microcircuits in olfactory cortex. *Neuron* **67**:452–465. doi:10.1016/j.neuron.2010.06.029

Sturm J, Nguyen T, Kandler K. 2014. Development of intrinsic connectivity in the central nucleus of the mouse inferior colliculus. *J Neurosci Off J Soc Neurosci* **34**:15032–15046. doi:10.1523/JNEUROSCI.2276-14.2014

Taniguchi H, He M, Wu P, Kim S, Paik R, Sugino K, Kvitsiani D, Kvitsani D, Fu Y, Lu J, Lin Y, Miyoshi G, Shima Y, Fishell G, Nelson SB, Huang ZJ. 2011. A resource of Cre driver lines for genetic targeting of GABAergic neurons in cerebral cortex. *Neuron* **71**:995–1013. doi:10.1016/j.neuron.2011.07.026

Tremblay R, Lee S, Rudy B. 2016. GABAergic Interneurons in the Neocortex: From Cellular Properties to Circuits. *Neuron* **91**:260–292. doi:10.1016/j.neuron.2016.06.033

898 Tyner CF. 1975. The naming of neurons: applications of taxonomic theory to the study of cellular
899 populations. *Brain Behav Evol* **12**:75–96.
900 Wallace ML, Saunders A, Huang KW, Philson AC, Goldman M, Macosko EZ, McCarroll SA, Sabatini BL.
901 2017. Genetically Distinct Parallel Pathways in the Entopeduncular Nucleus for Limbic and
902 Sensorimotor Output of the Basal Ganglia. *Neuron* **94**:138-152.e5.
903 doi:10.1016/j.neuron.2017.03.017
904 Wallace MN, Shackleton TM, Palmer AR. 2012. Morphological and Physiological Characteristics of
905 Laminar Cells in the Central Nucleus of the Inferior Colliculus. *Front Neural Circuits* **6**.
906 doi:10.3389/fncir.2012.00055
907 West MJ, Slomianka L, Gundersen HJ. 1991. Unbiased stereological estimation of the total number of
908 neurons in thesubdivisions of the rat hippocampus using the optical fractionator. *Anat Rec*
909 **231**:482–497. doi:10.1002/ar.1092310411
910 Willard FH, Ryugo DK. 1983. Anatomy of the central auditory system In: Willott JF, editor. The Auditory
911 Psychobiology of the Mouse. Springfield, Ill: C.C. Thomas. pp. 201–304.
912 Willott JF, Urban GP. 1978. Response properties of neurons in nuclei of the mouse inferior colliculus. *J*
913 *Comp Physiol* **127**:175–184. doi:10.1007/BF01352302
914 Winer JA, Larue DT, Diehl JJ, Hefti BJ. 1998. Auditory cortical projections to the cat inferior colliculus. *J*
915 *Comp Neurol* **400**:147–174. doi:10.1002/(SICI)1096-9861(19981019)400:2<147::AID-
916 CNE1>3.0.CO;2-9
917 Winer JA, Schreiner C, editors. 2005. The inferior colliculus: with 168 illustrations. New York, NY:
918 Springer.
919 Wu SH, Ma CL, Kelly JB. 2004. Contribution of AMPA, NMDA, and GABA(A) receptors to temporal pattern
920 of postsynaptic responses in the inferior colliculus of the rat. *J Neurosci Off J Soc Neurosci*
921 **24**:4625–4634. doi:10.1523/JNEUROSCI.0318-04.2004
922 Young ED, Brownell WE. 1976. Responses to tones and noise of single cells in dorsal cochlear nucleus of
923 unanesthetized cats. *J Neurophysiol* **39**:282–300.
924 Zeng H, Sanes JR. 2017. Neuronal cell-type classification: challenges, opportunities and the path
925 forward. *Nat Rev Neurosci* **18**:530–546. doi:10.1038/nrn.2017.85
926